nature biomedical engineering

ARTICLES

https://doi.org/10.1038/s41551-018-0334-7

Solid stress in brain tumours causes neuronal loss and neurological dysfunction and can be reversed by lithium

Giorgio Seano[1,2,12], Hadi T. Nia[1,12], Kyrre E. Emblem[3,12], Meenal Datta[1,4], Jun Ren[1], Shanmugarajan Krishnan[1], Jonas Kloepper[1], Marco C. Pinho[5], William W. Ho[1,6], Mitrajit Ghosh[1], Vasileios Askoxylakis[1], Gino B. Ferraro[1], Lars Riedemann[1], Elizabeth R. Gerstner[7], Tracy T. Batchelor[7], Patrick Y. Wen[8], Nancy U. Lin[9], Alan J. Grodzinsky[10], Dai Fukumura[1], Peigen Huang[1], James W. Baish[11], Timothy P. Padera[1], Lance L. Munn[1] and Rakesh K. Jain[1*]

The compression of brain tissue by a tumour mass is believed to be a major cause of the clinical symptoms seen in patients with brain cancer. However, the biological consequences of these physical stresses on brain tissue are unknown. Here, via imaging studies in patients and by using mouse models of human brain tumours, we show that a subgroup of primary and metastatic brain tumours, classified as nodular on the basis of their growth pattern, exert solid stress on the surrounding brain tissue, causing a decrease in local vascular perfusion as well as neuronal death and impaired function. We demonstrate a causal link between solid stress and neurological dysfunction by applying and removing cerebral compression, which respectively mimic the mechanics of tumour growth and of surgical resection. We also show that, in mice, treatment with lithium reduces solid-stress-induced neuronal death and improves motor coordination. Our findings indicate that brain-tumour-generated solid stress impairs neurological function in patients, and that lithium as a therapeutic intervention could counter these effects.

Brain tissue compression and deformation by a tumour mass is believed to be a major cause of the life-threatening neurologic symptoms seen in patients with brain cancer. Brain tissue can be deformed and its function perturbed by two mechanical forces: tumour-associated edema and solid stress[1]. Solid stress refers to the compressive and tensile mechanical forces exerted by the solid components of the tissues, such as cells and extracellular matrix[2–4]. Solid stress, its origin and its biological consequences are distinct from the fluid pressure that leads to edema, a well-studied mechanical abnormality in brain tumours[5,6]. Although the genesis and consequences of intratumour solid stress have been initially studied[3,4,6], details of the mathematically predicted[7] solid stresses have not been characterized in vivo, and they may have important consequences for the physiology of the normal brain surrounding the tumour. Moreover, no studies have been able to distinguish the mechanical effects from biological interactions between the tumour and normal brain tissue in vivo.

As a tumour grows in the cranium, it must displace or replace the surrounding tissue. The tumour growth-induced deformation of the brain—the so-called 'mass effect'—can cause severe disability or death, and represents a negative prognostic factor[8]. Although the neurological consequences of the mass effect are empirically known from the clinical management of patients, the mechanical features, magnitudes and biological consequences of the solid stresses from brain tumours remain unknown. The growth pattern of brain tumours (that is, nodular versus infiltrative) has been implicated as one of the potential determinants of the intratumour solid stress[4]. It is unclear, however, how different tumour growth patterns affect the physiological functions of the surrounding tissue. As a consequence of this lack of mechanistic insight and characterization, effective therapeutic strategies aimed at neuroprotection and alleviation of neurological impairment caused by abnormal compressive forces in the brain are currently unknown.

In this study, we utilized multiple orthotopic mouse models of primary and metastatic brain tumours, a custom-designed in vivo compression apparatus to distinguish the mechanical effects from biochemical interactions between the tumour and normal brain tissue, mathematical modelling and intravital microscopy to establish a causal link between solid stress and neurological dysfunction in the surrounding brain. We show that solid stresses are higher around nodular tumours than around infiltrative tumours, and they deform the surrounding brain tissue and neuronal nuclei, thus reducing peritumoural vascular perfusion and inducing neuronal loss.

[1]Edwin L. Steele Laboratories, Department of Radiation Oncology, Massachusetts General Hospital, Harvard Medical School, Boston, MA, USA. [2]Institut Curie Research Center, PSL Research University, Inserm U1021, CNRS UMR3347, Orsay, France. [3]The Department of Diagnostic Physics, Division of Radiology and Nuclear Medicine, Oslo University Hospital, Oslo, Norway. [4]Department of Chemical and Biological Engineering, Tufts University, Medford, MA, USA. [5]Department of Radiology, UT Southwestern Medical Center, Dallas, TX, USA. [6]Department of Chemical Engineering, Massachusetts Institute of Technology, Cambridge, MA, USA. [7]Stephen E. and Catherine Pappas Center for Neuro-Oncology, Department of Neurology, Massachusetts General Hospital, Harvard Medical School, Boston, MA, USA. [8]Department of Neuro-Oncology, Dana-Farber/Brigham and Women's Cancer Center, Harvard Medical School, Boston, MA, USA. [9]Department of Medical Oncology, Dana-Farber Cancer Institute, Harvard Medical School, Boston, MA, USA. [10]Center for Biomedical Engineering, Departments of Mechanical, Electrical and Biological Engineering, Massachusetts Institute of Technology, Cambridge, MA, USA. [11]Department of Biomedical Engineering, Bucknell University, Lewisburg, PA, USA. [12]These authors contributed equally: Giorgio Seano, Hadi T. Nia, Kyrre E. Emblem *e-mail: jain@steele.mgh.harvard.edu

In concert with our preclinical findings, we also discovered that stratification of patients based on initial tumour nodularity and perfusion impairment assessed with magnetic resonance imaging (MRI) from patients with glioblastoma (GBM) or breast cancer (BC) brain metastases was able to predict functional status at the time of diagnosis. Finally, lithium—a neuroprotective drug—strongly attenuates compression-induced neuronal damage in mice when administered as either a preventive or intervention agent. This indicates that protecting brain tissue from the solid stress-induced dysfunction is pharmacologically possible, and suggests a rapidly translatable use of neuroprotective agents to improve the quality of life in patients with nodular brain tumours.

Results

Measuring how nodular tumours mechanically affect the surrounding brain tissue. Little is known about how the tumour growth pattern observed in patients—nodular versus infiltrative—affects the magnitude, localization and consequences of tumour-generated solid stress exerted on the surrounding brain tissue. Nodular tumours have well-defined margins, while infiltrative tumours invade into the surrounding tissue as individual cells (Supplementary Fig. 1a). As a proof-of-concept study, we orthotopically implanted the nodular U87 cells and the highly infiltrative MGG8 GBM cells in nude mice. After 20 days of growth, we measured the solid stress in the tumours and surrounding tissue using a planar-cut method[4,9]. Briefly, we removed the brain, and then released the residual solid stress by transversally cutting the brain and the tumour at the plane of interest (Supplementary Fig. 1b). We measured the tissue deformation caused by the release of solid stress (Fig. 1a) as well as the Young's modulus (stiffness) of the tumour and the brain tissue (Supplementary Fig. 1c). The solid stress and stiffness measurements were performed on ex vivo tissues, which may differ from those in the in vivo setting due to the presence of vascular and interstitial pressure (see Methods for a more detailed discussion). These measures of the tumour–brain construct were incorporated in a finite-element model to estimate the radial (compression) and circumferential (tension) components of the solid stress exerted on the surrounding normal brain by the tumour (Fig. 1b,c, Supplementary Video 1 and Methods). Our results showed gradients of compression and tension in the surrounding brain tissue, more prominent around the nodular than the infiltrative tumours. At the tumour–brain interface, the circumferential solid stress was 0.110 ± 0.005 kPa around nodular tumours—as opposed to 0.063 ± 0.004 kPa for infiltrative tumours (Fig. 1b)—and the radial solid stress was 0.020 ± 0.001 kPa around nodular tumours—as opposed to 0.014 ± 0.001 kPa for infiltrative tumours (Fig. 1c). The force exerted by the tumours consistently distorted the micro-anatomy of the surrounding brain tissue. Consistent with the measured forces, the nodular U87 tumours locally deformed the surrounding tissue, as previously shown in other organs[7], while the infiltrative MGG8 GBMs did not (Fig. 1d).

Deformation of brains in patients phenocopies murine findings. The solid stress-mediated deformation of the surrounding tissue observed in preclinical models may reflect the 'mass effect' macroscopically observed in radiological exams in brain tumour (that is, tumour-induced deformation of the brain). We therefore investigated the deformation of the brain anatomy in patients. MRI allowed us to longitudinally observe the tumour growth in patients with GBM. Initial evidence in a post-surgery cohort suggested that nodular tumours had a larger mass effect than infiltrative ones (Supplementary Fig. 2a and Supplementary Videos 2 and 3). To investigate the association between the mass effect and neurologic deficit, we correlated brain tumour growth patterns with pre-surgery Karnofsky performance scores (KPSs), a clinical index used to estimate functional impairment. We used contrast-enhanced (CE)-T1-weighted, T2-weighted and FLAIR images from MRI as well as the Visually Accessible Rembrandt Images (VASARI) criteria for characterization of tumour margins[10]. This allowed us to stratify a cohort of 64 pre-surgery, pre-treatment GBM patients using a scoring method for the definition of enhancing and non-enhancing margins (Fig. 1e). We discovered that patients with perfectly defined margins of the tumour (that is, nodular, 29.7% in our cohort) showed a lower pre-surgery KPS than patients with ill-defined margins (Fig. 1f). Stratification based on CE-T1 or T2- and FLAIR showed comparable results (Supplementary Fig. 2b). Importantly, the nodular and infiltrative cohorts did not differ in tumour (CE-T1) or edema (T2- and FLAIR) volume (Supplementary Fig. 2c), suggesting that the association between tumour growth pattern and KPS is independent from the well-known effect of peritumour edema. The significant difference in pre-operative KPS between nodular (median KPS = 80) and infiltrative tumours (median KPS = 90) was especially provocative, in light of previously reported differences between KPS measured pre- and post-surgical resection of the tumour, where we expect a complete removal of the solid stress caused by the tumour[11].

These findings from mouse models and humans (measurements of solid stress, deformation of the surrounding brain and the resulting functional impairments) suggest that nodular brain tumours—compared with those that are more infiltrative—exert significant chronic local compression and tension on the surrounding brain tissue and this may affect neurological function.

Nodular brain tumours impair vascular perfusion of adjacent normal tissue and neuronal function. To shed light on the consequences of the local tumour-generated solid stresses on the surrounding brain and to investigate the mechanopathological basis for the performance reduction in patients with nodular tumours, we assessed vascular perfusion in mice bearing GBM and BC brain metastasis. We previously demonstrated that solid stress compresses blood vessels within tumours[3,6,12] and predicted this in non-central nervous system (non-CNS) tissues[7]. Using Doppler optical coherence tomography (OCT[13]), we performed longitudinal high-resolution angiography in tumour-bearing live mice with transparent cranial windows. We observed that nodular brain tumours—U87 (GBM), GL261 (mouse GBM) and BT474 (BC) (Supplementary Fig. 1a)—gradually displaced the surrounding vascular architecture and impaired vascular perfusion by reducing vascular volume fraction and vessel diameters (Fig. 2a,b, Supplementary Fig. 3 and Supplementary Videos 4 and 5). Moreover, we observed that the reduction in perfusion in the brain tissue strongly correlated with the tumour volume in nodular models (Supplementary Fig. 4a). Notably, the infiltrative MGG8 GBMs did not cause vascular perfusion reduction in the surrounding brain tissue (Fig. 2b and Supplementary Fig. 3a).

To investigate the effect of mechanical stress on normal brain tissue at the cellular level, we imaged blood flow and tumour cells intravitally and longitudinally using multiphoton microscopy. We observed that the nodular GL261 tumours deformed vessels and reduced the vascular area fraction and vessel diameters in the observed region at the border of the tumour, while the infiltrative MGG8 cells penetrated into the brain tissue without perturbing vascular architecture and vessel perfusion (Fig. 2c).

We then investigated the effects of mechanical stress on neurons in the surrounding brain tissue. Using intravital multiphoton microscopy, we imaged enhanced green fluorescent protein (EGFP)–H2B mice (which have GFP-positive nuclei) bearing *Discosoma* red fluorescent protein (DsRed)–GL261 tumours. Nuclei within the surrounding tissue were locally deformed (Fig. 3a), a potential consequence of compressive force. Solid stress compresses the cells, which transmit the compressive force to the nucleus, resulting in deformed nuclei. Since the intravital imaging

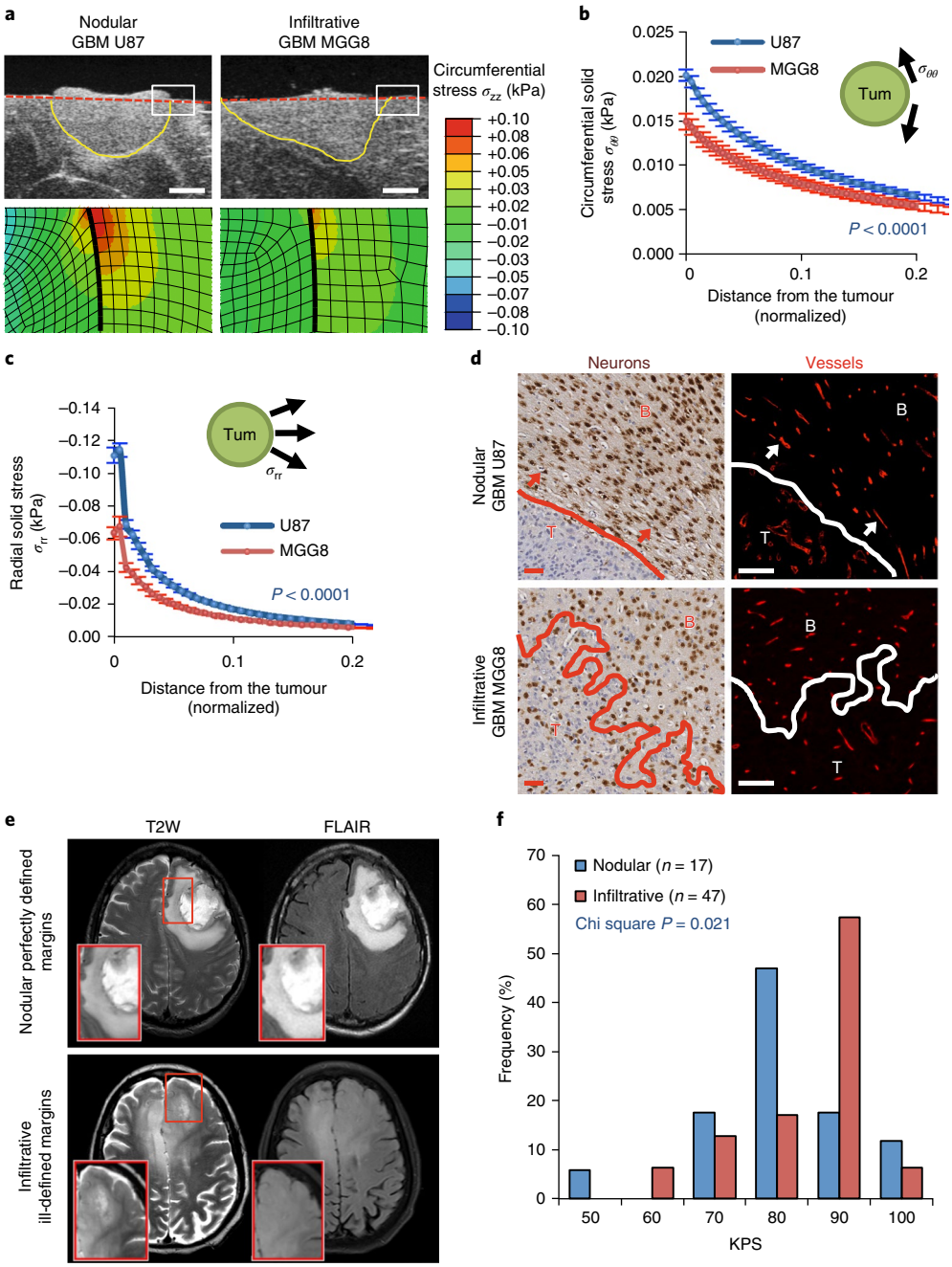

Fig. 1 | Measuring how nodular tumours mechanically affect the surrounding brain. a–c, Solid stress in mouse models of nodular (patient-derived U87 cell line) and infiltrative brain tumours (patient-derived MGG8 cell line) in nude mice. **a**, High-resolution ultrasound imaging of the stress-induced deformation and representative stress profiles across the tumour diameter and the normal surrounding tissue. Scale bars, 1 mm. **b**,**c**, Estimation of the circumferential (compression; $\sigma_{\theta\theta}$) and radial (tension; σ_{rr}) stress in the surrounding tissue obtained from mathematical modelling (described in Supplementary Fig. 1b–d and Methods). The data are the mean of three independent tumours ± s.e.m. Tum, tumour. **d**, Micro-anatomic deformation of the brain tissue around nodular tumours. IHC of U87 and MGG8 tumours at the interface of the normal brain tissue (neurons, NeuN staining; vessels, collagen IV staining). The arrows indicate the deformed region around the tumour; neurons are packed and vessels are displaced following the circumference of the tumour margin. T, tumour; B, brain. Representative images from a cohort of ten mice with a tumour are shown. Scale bars, 50 µm. **e**, Representative T2-weighted (T2W) and FLAIR MRI of pre-surgery pre-treatment patients with GBM with perfectly defined (nodular) and ill-defined (infiltrative) margins. **f**, KPS histograms of patients with perfectly defined margins (nodular) or ill-defined GBM (infiltrative). The results are from a cohort of 64 pre-surgery pre-treatment GBM patients.

of our reporter mouse model was not able to distinguish between neurons and the rest of the brain stromal cells, we performed immunohistochemistry (IHC) to stain the neuronal nuclei around nodular tumours. We observed the same nuclear deformation and a gradient of nuclear area reduction in neurons in the tissue surrounding the nodular tumours (Fig. 3b,c and Supplementary Fig. 4b,c). Notably, no deformation or area reduction was detected in neuronal nuclei around infiltrative MGG8 tumours (Fig. 3b,c and Supplementary Fig. 4b,c). Compression of neurons has been shown to cause neural cell death in vitro[14,15]. Similarly, we detected signs of apoptosis in the tissue surrounding nodular tumours (Fig. 3d and Supplementary Fig. 4d).

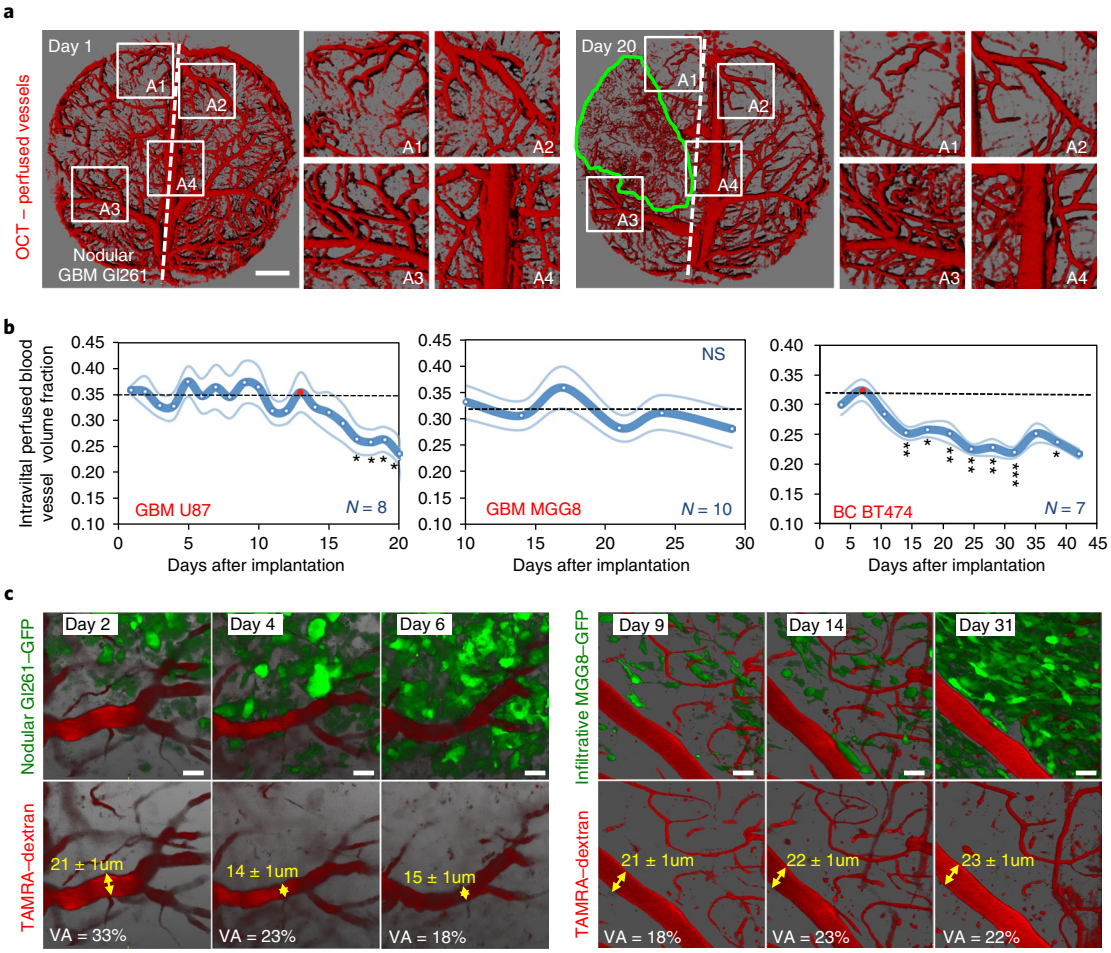

Fig. 2 | Reduced vessel perfusion in the brain tissue around nodular tumours. a, Longitudinal OCT intravital angiography (perfused vessels) of the nodular GI261 mouse model. U87 and BT474 are presented in Supplementary Fig. 3b,d. White dashed lines indicate the original position of the sagittal sinus, while the green line delimits the GL261 nodular tumour. Scale bar, 1 mm. **b**, Longitudinal quantitative analysis of the vascular perfused volume fraction in the surrounding tissue. GBM U87: day 17 $^{*}P = 0.025$ versus the red-dotted time point (day 13); day 18 $^{*}P = 0.011$; day 19 $^{*}P = 0.045$; day 20 $^{*}P = 0.037$. BC BT474: day 14 $^{**}P = 0.001$ versus the red-dotted time point (day 5); day 18 $^{*}P = 0.024$; day 21 $^{**}P = 0.003$; day 25 $^{**}P = 0.005$; day 28 $^{**}P = 0.001$; day 32 $^{***}P < 0.001$; day 38 $^{*}P = 0.035$. NS, not significant. The data are mean ± s.e.m. **c**, Intravital longitudinal multiphoton imaging depicting changes in vessel diameter in the nodular GI261–GFP and in the infiltrative MGG8–GFP GBM mouse models. GFP (green, tumour cells) and TAMRA–dextran (red, 2 MDa dextran, blood flow). VA, vascular area. Scale bars, 20 µm.

Collectively, these results indicate that nodular tumours—in comparison to infiltrative ones—locally reduce perfusion by compressing blood vessels in the surrounding brain tissue as well as by compressing neuronal nuclei and inducing neuronal loss.

GBM and BC patients with nodular tumours present reduced vascular perfusion in the surrounding brain tissue and neurologic dysfunction. To test whether our preclinical results on perfusion recapitulate those in patients, we investigated vascular perfusion in the surrounding normal-appearing tissues in a cohort of 64 pre-surgery GBM patients using MRI images. We assessed perfusion in the normal-appearing tissue, avoiding the regions of T2-weighted and FLAIR peritumoural edema and then normalizing with the whole-brain perfusion levels (which are different in each individual; Supplementary Fig. 5a). Our analysis showed that 53% of patients experienced a local gradient of reduced perfusion in the surrounding brain tissue (Fig. 4a,b). We also confirmed these perfusion results in an additional independent cohort of 14 post-surgery, but otherwise untreated, GBM patients (Supplementary Fig. 5b–e).

The above imaging method allowed us to stratify the patients from our pre-surgery cohort on the basis of their level of perfusion in the surrounding tissue (that is, 'reduced perf' or 'unchanged perf'). Patients with reduced perfusion in the surrounding tissue had significantly poorer KPS (Fig. 4c). Notably, these two patient cohorts showed similar levels of tumour volume and edema (Fig. 4d) and had equal pre-treatment with steroids (Supplementary Fig. 6a). Moreover, diffusion tensor imaging MRIs displayed local deformation of the white matter anatomy in the surrounding brain tissue (Fig. 4b), as previously shown[16]. We observed that the tumours with local reduction of perfusion ('reduced perf') were more often classified as nodular (Fig. 4e and Supplementary Fig. 6b), but no difference in the tumour shape was detected (Supplementary Fig. 6c,d).

As metastases in the brain are reported to be primarily nodular[17], we then analysed a cohort of 34 patients with BC metastases in the brain with the same imaging approach as described above. Indeed, we observed markedly reduced perfusion in the surrounding tissue in proximity to the tumour (Fig. 4f,g and Supplementary Fig. 6e). These results indicate that both primary and metastatic nodular tumours locally reduce vascular perfusion in the surrounding brain tissue and that this is correlated with neurological impairment.

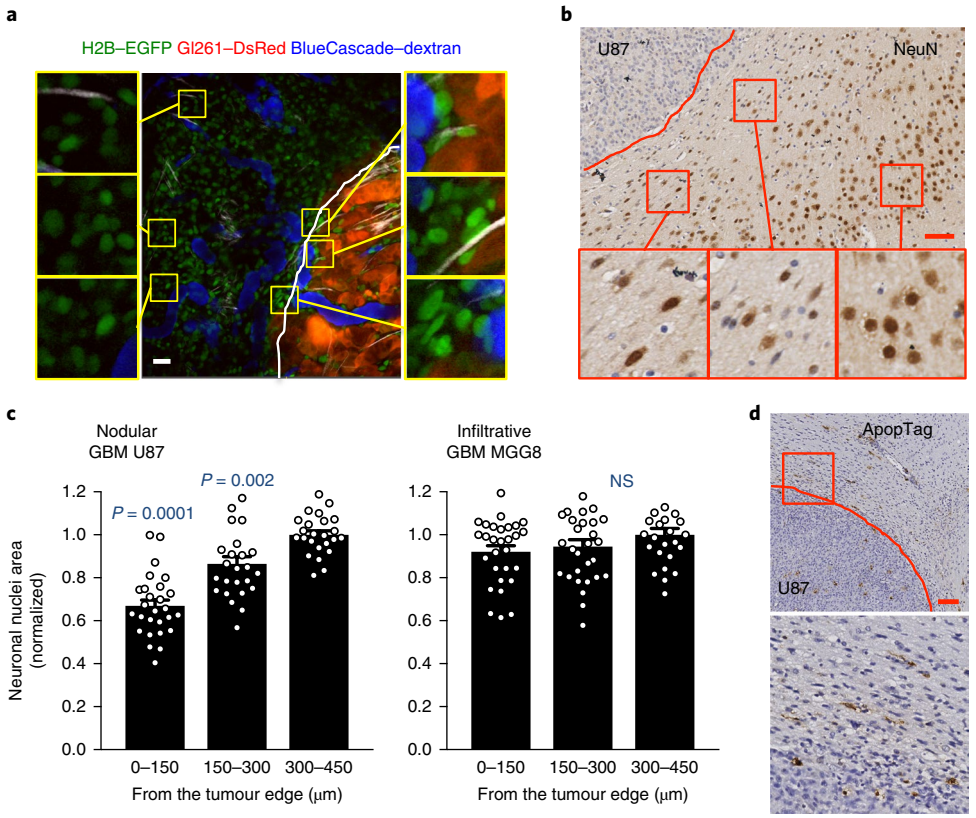

Fig. 3 | Neuronal deformation and death in the brain tissue around nodular tumours. a, Intravital multiphoton imaging of brain nuclei around the nodular mouse GI261-DsRed GBM implanted in H2B-EGFP mouse (CAG::H2B-EGFP C57/BL6). GFP (green, nuclei within the brain tissue), DsRed (red, tumour cells) and CascadeBlue (blue, 2 MDa dextran, blood flow). The insets are magnifications of the yellow squares. Scale bar, 20 μm. **b**, IHC of neuronal nuclei (NeuN) in the surrounding brain tissue of mice with the nodular U87 tumour. A representative image from a cohort of ten mice with a tumour is shown. The insets are magnifications of the red squares. Scale bar, 50 μm. **c**, Quantification of neuronal nuclear area in the brain tissue around nodular or infiltrative tumours. The data are mean ± s.e.m. *P* values are versus '300–450 from the tumour edge'. **d**, Apoptosis (ApopTag) at the interface between the nodular U87 tumour and the normal brain tissue. A representative image from a cohort of ten mice with a tumour is shown. The bottom panel is a magnification of the red square. Scale bar, 100 μm.

In vivo solid stress application impairs vascular perfusion and induces neuronal dysfunction. Taken together, the above results in preclinical and clinical settings demonstrate a strong association between the gradient of solid stress and the reduction in local vessel and neural function in the surrounding brain tissue. To mechanistically confirm this link and distinguish the mechanical effects from biological interactions between the tumour and normal brain tissue (for example, cytokines and inflammation associated with cancer cells that are cytotoxic to normal cells[18]), we directly and chronically applied mechanical compression to the brains in living mice with no tumour. This also avoided the confounding effect of the peritumoural edema. Our custom-designed in vivo apparatus was composed of a set screw mounted on a modified cranial window and separated from the brain tissue by a biocompatible and deformable membrane. By turning the screw into the cranial window in nude mice without tumour, we can control the displacement of brain tissue so that it resembles that caused by nodular tumours (Fig. 5a and Supplementary Fig. 7a). We expanded the compressing volume at around 1.3 $mm^3 d^{-1}$ for 14 days and reached a maximum volume of approximately 19.0 ± 0.7 mm^3. The rate of compression was comparable to the rate of growth in the nodular U87 and BT474 intracranial models over the same time period, while the maximum volume was less than the tumours at the end point (Supplementary Fig. 7b). This method gradually and chronically compressed the brain and deformed the micro-anatomy of the cortex (Fig. 5b and Supplementary Fig. 7c) mimicking the effects of a nodular tumour (Fig. 1d). We then performed longitudinal angiography on mice with controlled and gradual compression on the brain and discovered that vascular perfusion and vessel diameter were reduced (Fig. 5c and Supplementary Fig. 7d), confirming our observation in nodular tumour-bearing brains (Fig. 2a,b).

Next, we investigated the effects of compressive stresses on neurons and other cellular components in the brain. First, ultrastructure analysis revealed signs of cell distress (condensed chromatin) in the compressed cortices (Fig. 5d and Supplementary Fig. 7e). In addition, we discovered that the NeuN-positive neuronal nuclear area was significantly reduced and deformed. The total number, area and circularity of neuronal nuclei were substantially reduced in the cortex after chronic compression (Fig. 5e–g and Supplementary Fig. 8a). In the compressed cortices we also detected apoptosis, signs of degenerative autophagy (LC3-II-positive vesicles), reduction of oligodendrocyte processes ($CNPase^+$ filaments) and recruitment/activation of astrocytes (Supplementary Fig. 8b) and signs of necrosis (TNF-α and RIP1; Supplementary Fig. 8c), all indicating neuroinflammation and neuronal damage.

Neural damage in the motor and somatosensor cortex—the regions compressed with our device—may consequently impair sensorimotor coordination and balance in mice, mimicking the neurological impairment that commonly occurs in brain tumour patients. By using Rotarod and static gait tests (Supplementary Video 6 and refs. [19,20]), we found that motor coordination and locomotion was significantly reduced in mice where the cortex was compressed (Fig. 5h,i

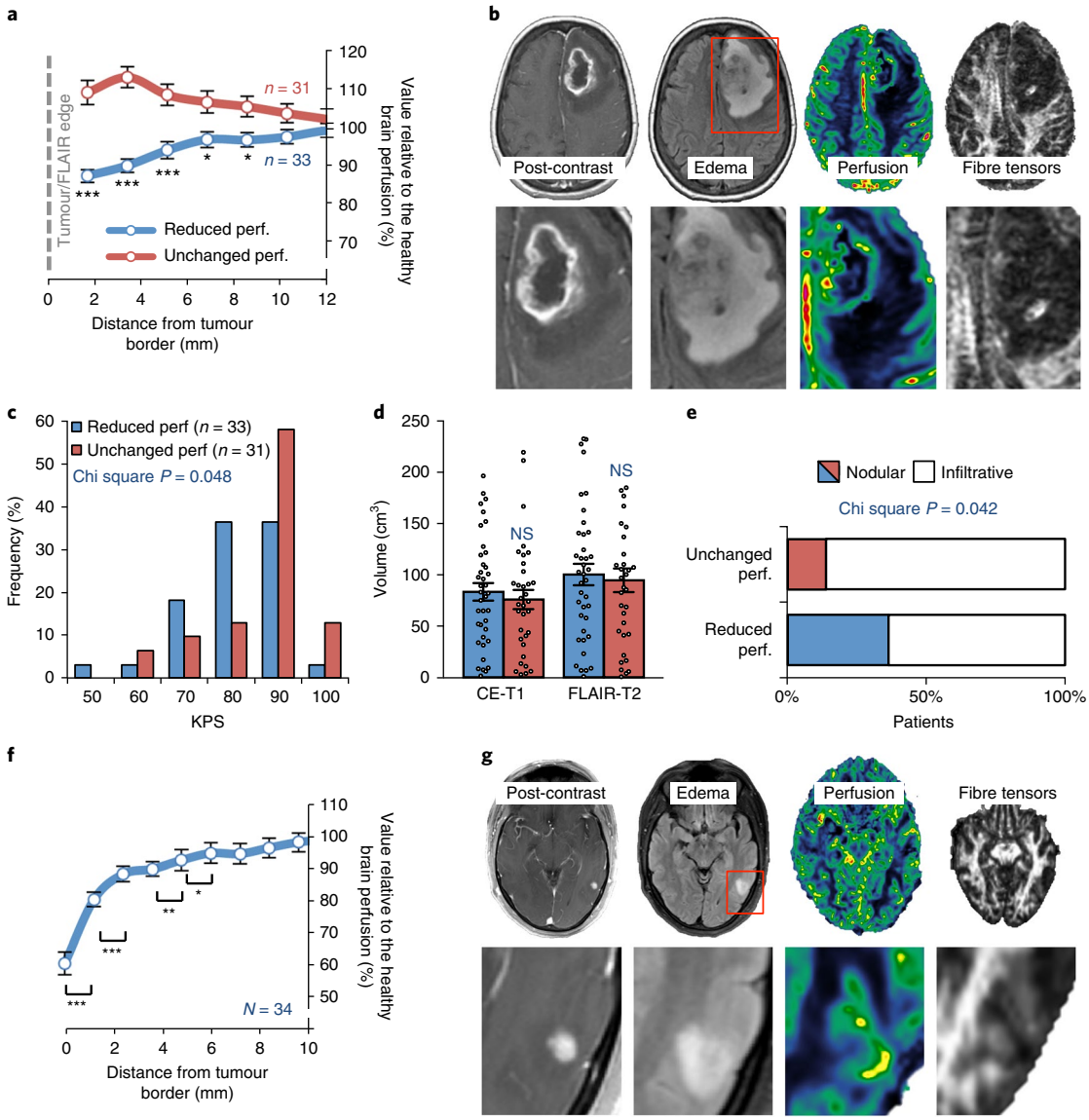

Fig. 4 | Reduced perfusion in the surrounding normal tissues in GBM and BC brain metastasis patients. a, Quantification of the local perfusion in surrounding normal brain tissue from immediately adjacent to the peri-edematous region of the GBM to the region 12 mm away from the tumour edge. The cohort of 64 pre-surgery GBM patients was divided into patients with a reduced perfusion in the surrounding tissue ('reduced perf') and patients with no difference in perfusion ('unchanged perf'). The data are mean ± s.e.m. Point 1.72: ***$P < 0.001$ versus 'unchanged perf'; point 3.44: ***$P < 0.001$; point 5.15: ***$P = 0.001$; point 6.87: *$P = 0.014$; point 8.59: *$P = 0.019$. **b**, A representative pre-surgery GBM patient from a cohort of 33 patients with local reduced perfusion and fibre tensor signal in the surrounding tissue as well as midline shift. **c**, Histograms of KPS in 'reduced perf' and 'unchanged perf' GBM patients. **d**, CE-T1 and FLAIR (and T2-weighted) volumes in the two classes with 'reduced perf.' or 'unchanged perf.' in the surrounding brain tissue. The data are mean ± s.e.m ($N = 64$ patients). **e**, Classification of the patients in the two perfusion subclasses is based on the edematous ('FLAIR-T2') MRI margins ($n = 64$ patients). A comparable result was obtained with CE-T1 MRI (Supplementary Fig. 6b). **f**, Quantification of the local perfusion in the brain tissue immediately surrounding the BC brain metastases. The results are from a cohort of 34 BC patients (26 HER2-positive; 8 HER2-negative). The data are mean ± s.e.m. Point 0: ***$P < 0.001$ versus point 1.2; point 1.2: ***$P < 0.001$ versus point 2.4; point 3.6: **$P = 0.010$ versus point 4.8; point 4.8: *$P = 0.013$ versus point 6. **g**, A representative BC HER2-negative patient from a cohort of 34 patients with local reduction of perfusion and fibre tensor signal in the surrounding tissue.

and Supplementary Fig. 8d,e). The mice undergoing brain compression maintained normal body weight (Supplementary Fig. 8f).

These findings mechanistically explain the results shown in patients and mice with nodular tumours (Figs. 1 and 3) and the clinical evidence of the correlation of the mass effect events with performance in patients. The human brain has been shown to have a pronounced compression–tension asymmetry[21] and heterogeneity in its stiffness[22,23], as well as a broad spectrum of functions for each specific brain region. Consequently, we expect that the local compression of different areas of the brain might trigger different mechanical and neurological responses from the brain tissue. Therefore, further studies are needed to assess the regional effects of local solid stress from brain tumours.

In vivo removal of solid stress restores vascular perfusion and neurological function. Next, we asked whether the release of compression—simulating clinical surgical resection—leads to the rescue of the biological consequences of solid stress. First, we investigated

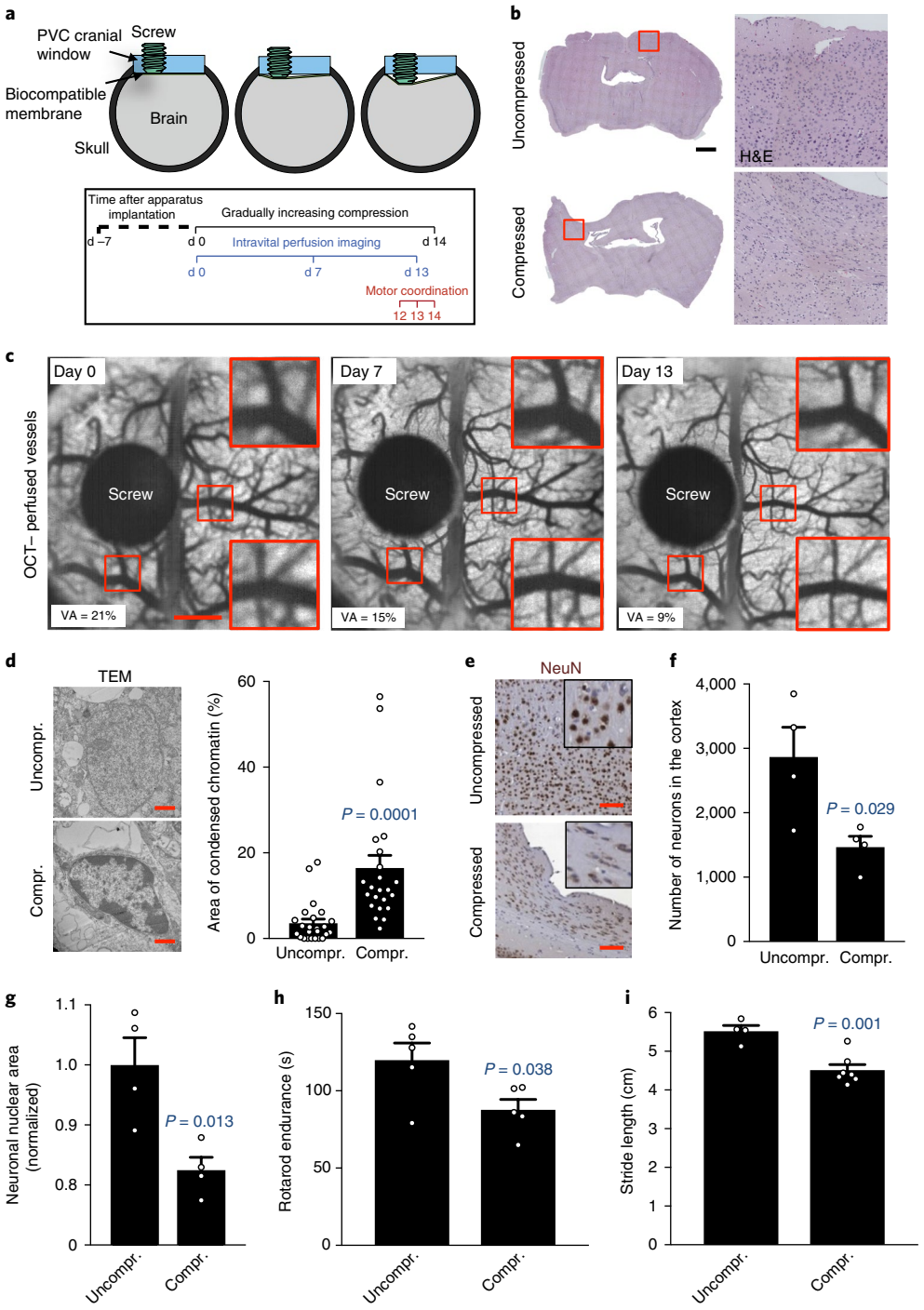

Fig. 5 | Direct chronic compression of the brain reduces vessel perfusion and induces neuronal damage. a, Schematic of the intravital compression device procedure. **b**, Deformation of the compressed tissue. H&E staining of the whole brain gradually and chronically compressed for 14 days. A representative image from a cohort of seven mice with the compression device is shown. Insets are magnifications of the red squares. Scale bar, 1 mm. **c**, OCT longitudinal intravital angiography of the brain seen through the compression apparatus (average projection of the 3D imaging). VA is the quantification (%) of the shown images. Scale bar, 1 mm. **d**, Left, ultrastructural imaging of nuclei in uncompressed and compressed cortices via electron microscopy. Representative images from a cohort of three mice per experimental point are shown. Scale bars, 1 µm. Right, quantification of the percentage of condensed chromatin area in *n* nuclei. The data are mean ± s.e.m. **e**,**f**, NeuN (neuron nuclei) in the compressed cortex. Representative images from a cohort of four mice per experimental point (**e**) and quantification of the number of neurons ($NeuN^+$ nuclei) per cortex exposed to the cranial window (**f**) are shown. The data are mean ± s.e.m. Scale bar, 100 µm. **g**, Quantification of neuronal nuclear area in uncompressed or compressed cortices. Normalized results are shown. The data are mean ± s.e.m. **h**, Rotarod endurance (index of motor coordination and balance) after 14 days of compression of the motor and somatosensory cortex. The data are the mean of thee consecutive days (one measure per day) and five mice per group ± s.e.m. **i**, Static gait test (index of locomotion); footprint analysis of the stride length. The footprint results are shown in Supplementary Fig. 8e. The data are the mean for three technical replicates and *n* mice per group ± s.e.m.

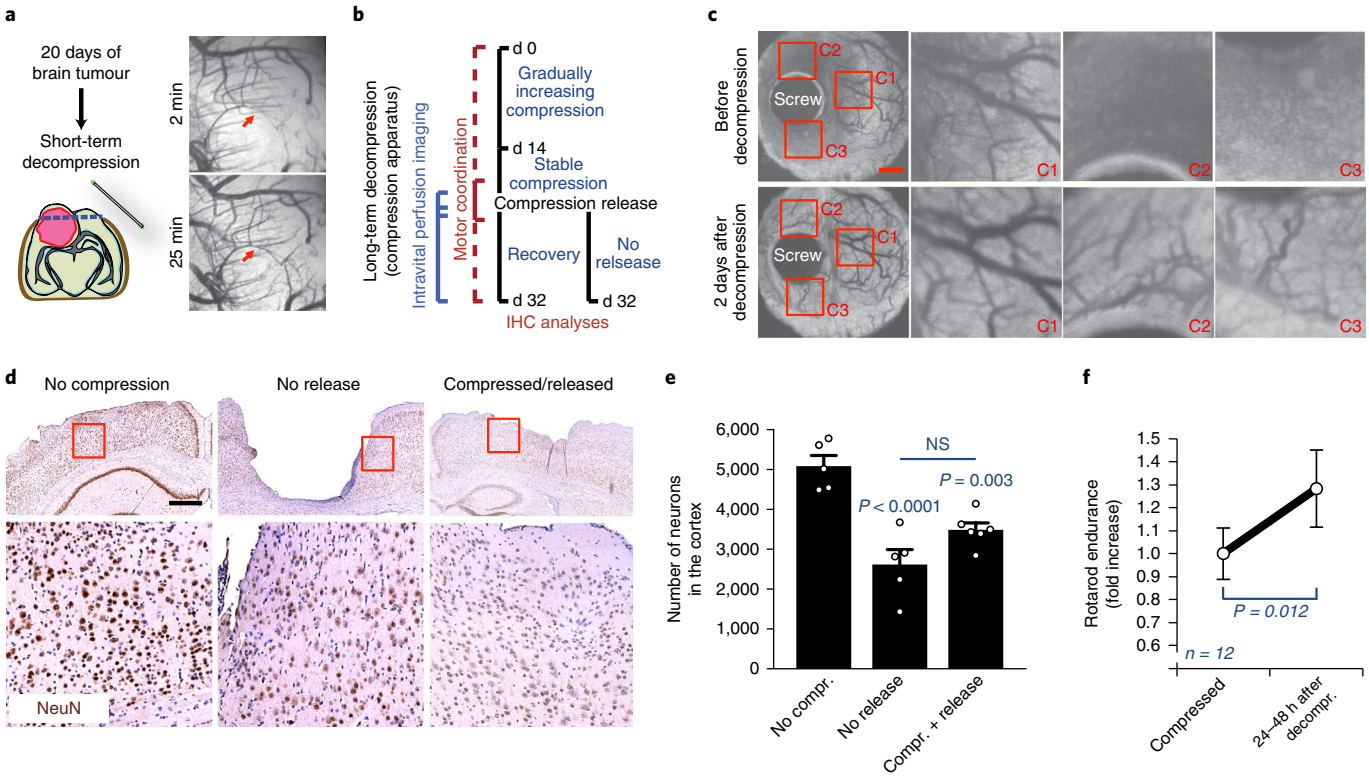

Fig. 6 | Decompression restores vessel perfusion and partially rescues motor coordination. a, OCT angiography after decompression of brains with nodular U87 tumours by removing the cranial window (craniotomy). Red arrows indicate blood vessels increasing their diameter during decompression. The complete time course is shown in Supplementary Fig. 9b,c. **b**, Schematic of the long-term compression/decompression timeline via the in vivo chronic apparatus. **c**, Longitudinal OCT angiography before and after decompression. Images of a representative mouse from a cohort of three mice. The insets are magnifications of the red squares. See Supplementary Video 7 for the complete time-lapse sequence. Scale bar, 1 mm. **d**, Representative cortices stained with anti-NeuN from a cohort of three mice. The long-term compression induces tissue loss and the decompression partly restores the micro-anatomy of the cortex. The insets are magnifications of the red squares. Scale bar, 500 µm. **e**, Quantification of the NeuN$^+$ neurons in the cortices, not compressed or compressed and released. The data are mean ± s.e.m. **f**, Rotarod endurance (index of motor coordination and balance) 24–48 h after decompression of the motor and somatosensory cortex. The data are the mean of 2 consecutive days and 12 mice per group ± s.e.m (normalized with the value before decompression).

a short-term decompression in brains compressed by a nodular tumour. After 20 days of nodular tumour growth in the brain of nude mice, we decompressed the brains by removing the cranial windows, mimicking craniotomy or surgical resection where consequent displacement has previously been shown[24,25]. Thus, instead of a full surgical resection that would damage the surrounding tissue, this approach allowed us to partially release the tumour compressive forces and investigate intravital brain vessel perfusion. We observed a strong increase in perfusion in the surrounding brain after alleviation of the tumour-induced compressive forces (Fig. 6a and Supplementary Fig. 9a–c).

Using the in vivo compression device in mice with no tumour, we next investigated whether the removal of solid stress—modelling a full tumour resection—leads to the restoration of vascular perfusion, neuronal damage and motor coordination (Fig. 6b). Removing solid stress after long-term compression—achieved by turning the screw backwards toward its original set-point—restored vascular perfusion (Fig. 6c, Supplementary Fig. 9d and Supplementary Video 7). Histological analysis of cortices after 32 days of compression (long-term) showed massive brain tissue loss in the compressed area (Fig. 6d). Interestingly, two weeks after decompression, the brain showed a partial restoration of the micro-anatomy and number of neuronal cells (Fig. 6d,e and Supplementary Fig. 10a). The release of the compression significantly improved motor coordination at two days after decompression (Fig. 6f)—in line with previous data in post-surgery GBM patients[11]. However, motor coordination then dropped back again (Supplementary Fig. 10b), indicating an incomplete recovery.

These results allowed us to decouple the tumour mechanics from the biological interactions between the tumour and the surrounding normal tissue, thus mechanistically showing that both perfusion and neuronal function are impaired by solid stress and may be partially restored when the solid stress is removed, as occurs during surgical resection of the tumour[25].

Systemic treatment with lithium protects neurons from solid stress-induced neuronal death and neurological dysfunction. To reduce the compression-induced neuronal damage and further improve neurological ability, we tested potential neuroprotective therapeutic strategies aimed at preserving neuronal function in chronically compressed brain tissues. The compression device allowed us to screen multiple drugs in a single animal study. We systemically treated mice with the following drugs during the chronic/gradual compression and the following two weeks after decompression (Fig. 7a): necrostatin-1 (7 mg kg^{-1} d^{-1} i.p.; similar to ref. [26]), valproic acid (400 mg kg d^{-1} i.p.[27]), lithium chloride (50 mg kg^{-1} d^{-1} i.p.[28]) and dexamethasone (a single dose at maximum compression as shown in Supplementary Fig. 10d, 10 mg kg^{-1} i.p.[29,30]). These agents are known to cross the blood–brain barrier[31–33], and have been shown to be neuroprotective during CNS ischaemia or

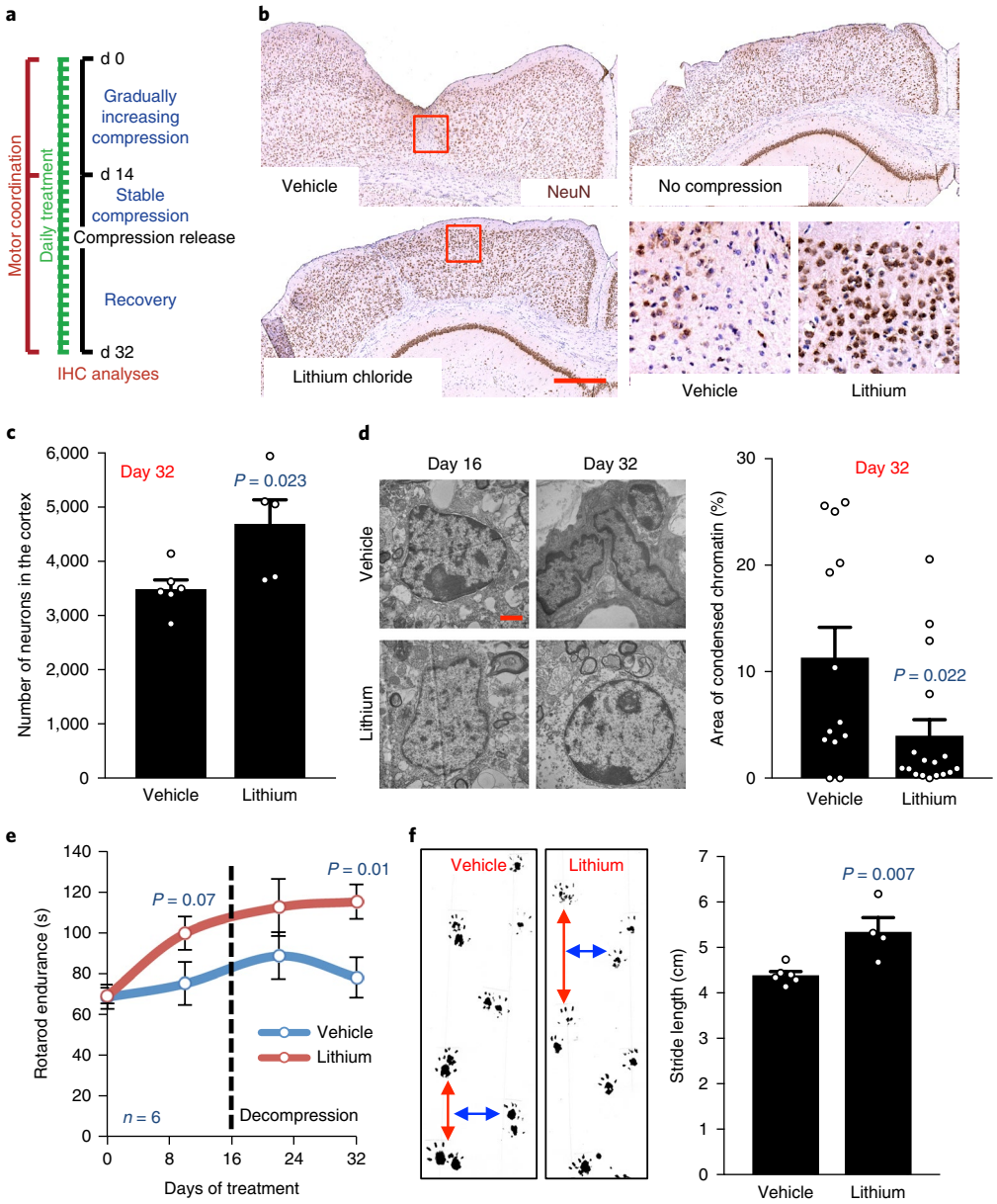

Fig. 7 | Systemic treatment with lithium alleviates compression-mediated neuronal damage. a, Schematic of the treatments in the long-term compression/decompression procedure. **b**, Representative cortices stained with anti-NeuN from a cohort of five mice per experimental point. Chronic lithium treatment preserves the cortex micro-anatomy after decompression. The insets are magnifications of the red squares. Scale bar, 500 µm. **c**, Quantification of the NeuN$^+$ neurons in the cortices, compressed and released. The data are mean ± s.e.m. **d**, Left, ultrastructural imaging of nuclei in compressed cortices treated with vehicle or lithium via electron microscopy. Representative images from a cohort of three mice per experimental point are shown. Scale bar, 1 µm. Right, quantification of the percentage of condensed chromatin area in *n* nuclei. The data are mean ± s.e.m. **e**, Longitudinal analysis of the Rotarod endurance (index of motor coordination and balance). The data are the mean of two consecutive days and six mice per group ± s.e.m. *P* values are Vehicle versus Lithium. **f**, Static gait test (index of locomotion); footprint analysis of the stride length at the time of highest compression (day 14). The data are the mean of three technical replicates and *n* mice per group ± s.e.m. A total of 115 steps were measured for vehicle-treated mice and 62 for lithium-treated ones.

neurodegeneration[26–28]. No body weight loss was detectable in mice after one month of treatment (Supplementary Fig. 10c), indicating no evident toxicity of the drugs. Our results identified lithium as a potential neuroprotective agent, while necrostatin-1, valproic acid and dexamethasone showed no evident neuroprotective improvement in our experimental setting (Supplementary Fig. 10c–e). We replicated the compression/release experiment under lithium treatment (Fig. 7a), and found that lithium significantly reduced neuronal death, and massively attenuated the reduction of cortical tissue area in the compressed brains (Fig. 7b,c). Moreover, ultrastructure analysis qualitatively showed reduced condensed chromatin (a sign of cell distress) in the lithium-treated cortices (Fig. 7d). As a consequence, the Rotarod motor coordination in lithium-treated mice was improved during both the compression and decompression phases with 34% higher end-point endurance than in control mice (Fig. 7e and Supplementary Fig. 10f). Similar results were obtained with the static gait test (Fig. 7f and Supplementary Fig. 10g).

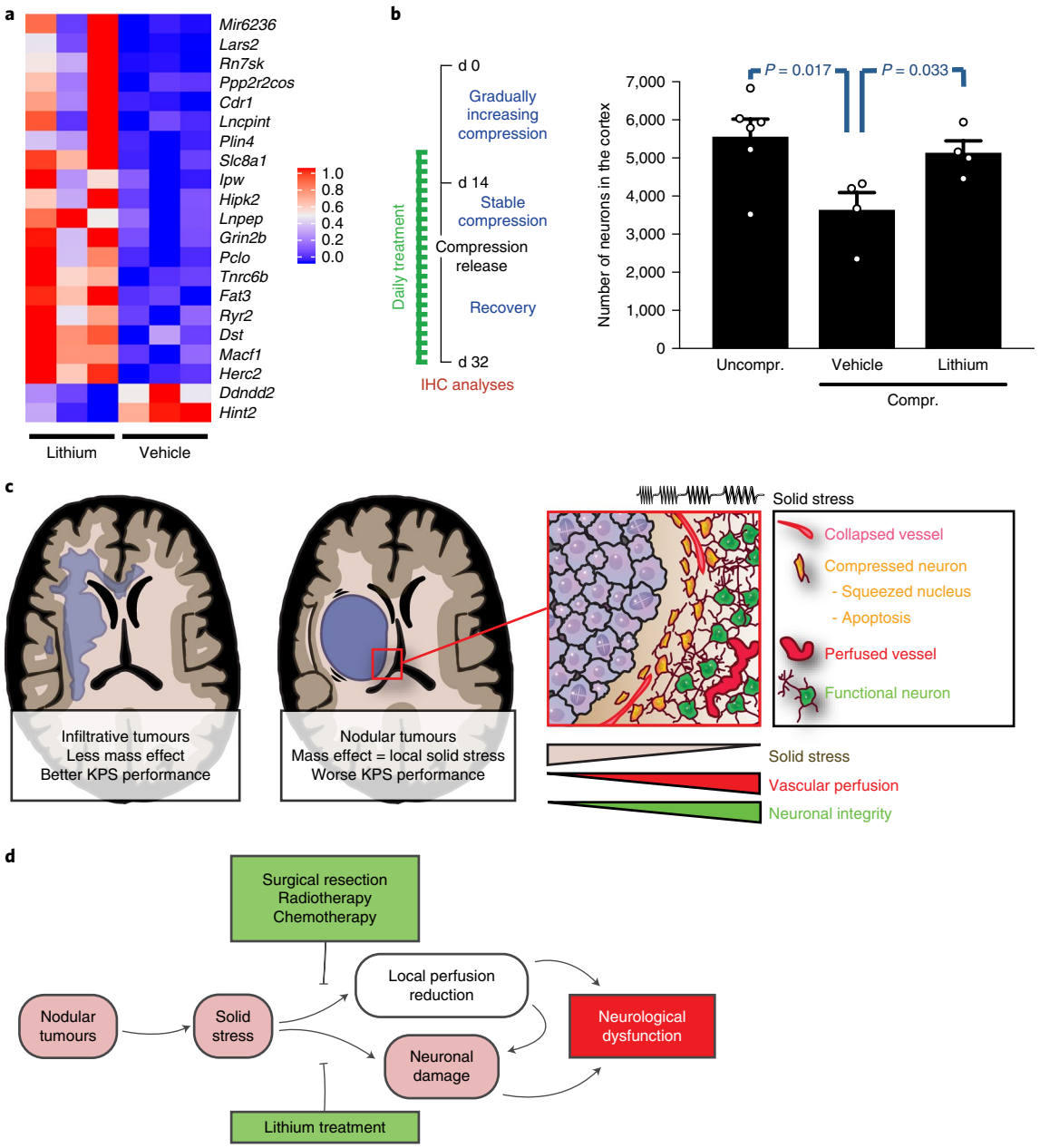

Fig. 8 | Solid stress from nodular brain tumours compresses the surrounding brain tissue, thus causing neurological dysfunction. a, A heatmap illustrating normalized gene expression of differentially expressed genes (FDR < 0.05) from RNA-Seq analysis of compressed/released cortices under chronic lithium treatment. **b**, Quantification of the NeuN$^+$ neurons in the cortices, compressed and released lithium-treated with treatment start when compression and symptoms were already present. The data are mean ± s.e.m. **c**, Schematic summarizing the effects of nodular tumours and their resulting solid stress on the surrounding brain tissue. Nodular tumours exertsolid stress to the surrounding brain tissue, with consequent reduction of vascular perfusion and neuronal functionality, while infiltrative tumours appeared to exert lower solid stress to the brain. **d**, Schematic summarizing the causes, modifiers and consequences of solid stress from nodular tumours.

To gain mechanistic insight into the neuroprotective effect of lithium, we performed bulk RNA-sequencing (RNA-Seq) on cortices that were compressed, released and chronically treated with lithium or vehicle (Fig. 7a). With a sample size of 3 per group, a total of 21 genes were differentially expressed in lithium-treated cortices versus vehicle control (Fig. 8a and Supplementary Tables 1 and 2; false discovery rate (FDR) < 0.05). Of the 21 differentially expressed genes, 19 were upregulated and 2 were downregulated in the cortices of lithium-treated mice (Fig. 8a, Supplementary Fig. 11a and Supplementary Tables 1 and 2). The function of these genes in the CNS were linked to ion channels, mitochondrial function and neuronal differentiation as well as protection from apoptosis, autophagy and ischaemia (Supplementary Tables 1 and 2). To systematically analyse our RNA-Seq results, we performed gene-annotation enrichment analysis using the DAVID Bioinformatics Resource[34]. Significantly upregulated gene ontologies in the lithium-treated group included dendrite, postsynaptic density, neuron projection (cellular components), protein binding (molecular function) and protein localization to synapse (biological process) (Supplementary Fig. 11b–e and Supplementary Data 1a). Functional annotation clusters associated with neurons, synapses, microtubules and calcium ion transport were also enriched in the

upregulated genes in the lithium-treated group (Supplementary Data 1b). Taken together, these results suggest that lithium treatment induces survival pathways in neurons (as demonstrated in Fig. 7b,c) and point out how lithium preserves neuronal function during the compression/release phase.

Finally, we tested whether lithium is neuroprotective if given when the compression and resulting neurological symptoms are already present in mice. Notably, in this more clinically relevant established compression model, lithium also efficiently increased the number of surviving neurons (Fig. 8b).

These results show the therapeutic potential of lithium in preserving neuronal and neurologic function in CNS affected by brain tumour-generated solid stress.

Discussion

Brain tumours, particularly GBM and brain metastases, have poor prognosis and are associated with significant morbidity due to progressive neurologic dysfunction. Although huge efforts have been employed to inhibit or stop brain tumour growth, little is known about the reasons for neuronal loss in the surrounding brain tissue, which is the ultimate cause of significant neurological dysfunction, loss of quality of life and eventually death. One of the possible causes of neuronal loss is the tumour-generated solid stress exerted on the surrounding brain tissue. We previously predicted solid stress in and around non-CNS tumours[7]. However, the growth pattern of the tumour (infiltrative versus nodular), the actual mechanical properties of the tissues and the impact on the brain function were not experimentally investigated previously. We therefore decided to examine the effects of the growth pattern on the solid stress applied to the surrounding brain tissue. Our results showed higher solid stress in the tissue around nodular than infiltrative tumours and this prompted us to investigate whether this has consequences for neurological function. We found neuronal damage and reduced perfusion around nodular tumours with corresponding neurological dysfunction (Fig. 8c). Importantly, these preclinical results allowed us to design a stratification method for GBM and BC patients with brain metastases using perfusion MRI, which can be used to predict which patients are likely to experience solid stress-mediated neurological impairment. We discovered an association between the growth pattern, reduced perfusion levels in the surrounding tissue and neurological impairment in a large set of patients across multiple cohorts. Notably, these associations were independent of peritumoural edema, widely recognized as an important determinant of neurological function in brain tumour patients, and treatment with steroids.

Using a custom-designed in vivo compression apparatus, we simulated the physical forces from nodular tumours exerted on the brain and we demonstrated a causal link between solid stress and a reversible reduction of vascular perfusion and semi-irreversible neurological dysfunction. Importantly, the neurons died as a consequence of the slow and chronic compression of the compression apparatus. This preclinical model allowed us to experimentally isolate the mechanical forces on the brain from other potential reasons of neuronal death and neurological dysfunction caused by brain tumours, such as excitotoxicity, inflammation, tumour release of neurotoxic factors and physical contact between tumour cells and normal brain. Moreover, we demonstrated that part of the dysfunction caused by the compression of the normal tissue could be rescued by the removal/release of solid stress, as happens during surgical resection, chemotherapy and radiotherapy. As removal is not sufficient to completely restore the cortex tissue and the neurological function (semi-irreversible effect), we therefore proposed the use of neuroprotective drugs to counter these effects.

Our results suggest lithium treatment as a potent neuroprotective therapeutic strategy in patients with nodular brain tumours, characterized by low perfusion in the surrounding tissue and lower KPS. For decades, lithium has been in use for psychiatric disorders, such as mania, depression and bipolar disorder. Notably, in our experiments the lithium dose administered here (50 mg kg^{-1}) was comparable to or lower than that given to mice in anti-depressant experiments (50–400 mg kg^{-1}; ref. [35]). In preclinical models and clinical studies, lithium has been proved to have neuroprotective effects in several neurodegenerative, brain-injury and ischaemic models[36–41] and this is in line with our RNA-Seq results. Notably, lithium also exerts anti-tumour effects by inhibiting tumour growth, chemosensitizing GBM preclinical models to temozolomide[42,43] and reducing invasion of cultured GBM cells[44], although its clinical efficacy remains to be determined in a clinical trial setting. These previous reports and our own findings support a potential therapeutic use of lithium in brain tumour patients.

Preservation of neurological function is increasingly taken into consideration in current clinical practice and neuro-oncologists now consider quality of life as a critical end point[45]. Our results now implicate solid stress as one of the causes of brain tumour-induced loss of neurological functions. Thus, our preclinical findings provide rigorous evidence for immediate translation of the concept of neuroprotection in the specific subclass of patients with nodular brain tumours who experience neurological defects due to the compression of the surrounding tissue. These agents can be used in addition to treatments that alleviate the tumour-generated mass effect to permit neuronal preservation while treatments to reduce tumour mass by surgery, radiation and chemotherapy are ongoing.

In conclusion, we showed that the compression-induced neuronal damage may be attenuated by decompression, mimicking surgical resection, and chronic systemic treatment with lithium (Fig. 8d). These results indicate neuroprotective treatments as potential therapeutic strategies in patients with nodular 'pushing' tumours to reduce the pathological effects of solid stress on the surrounding brain neurons, even in cases of inoperable or advanced brain cancer to improve quality of life for as long as possible.

Methods

Mice. All animal protocols were approved by and in accordance with the guidelines established by the Institutional Animal Care and Use Committee (IACUC) at Massachusetts General Hospital (MGH). The mouse colony (MGH Cox7) was maintained in accordance with National Institutes of Health and MGH guidelines. MGH is accredited with the International Association for Assessment and Accreditation of Laboratory Animal Care (AAALAC) and the NIH Office of Laboratory Animal Welfare (A3596-01). All experiments were performed in eight- to ten-week-old female nude mice. In the case of Fig. 3a, we used CAG::H2B–EGFP (C57/BL6) mice from Jackson Laboratory.

Reagents and cell culture. Lithium chloride (L4408), valproic acid sodium salt (P4543) and necrostatin-1 (N9037) were from Sigma.

The human U87 and BT474 cells were from ATCC and the mouse Gl261 cells were from the National Cancer Institute Repository. MGG8, a cell line derived from a GBM patient, was previously established in the Department of Neurosurgery at MGH[46]. MGG8 and Gl261 cells were grown in serum-free conditions using the NeuroCult NS-A proliferation kit (Stemcell Technologies)[47–49]. Both cell lines were stably transduced with GFP or dsRed using a lentiviral construct. U87 cells were cultured in DMEM with 10% (vol/vol) FBS. Human HER2-amplified BC BT474 cells were cultured in RPMI 1640 supplemented with 10% FBS (Atlanta Biologicals)[50]. All cell lines were repeatedly tested and were negative for mycoplasma using the Mycoalert Plus Mycoplasma Detection Kit (Lonza) and were authenticated before use by IDEXX Laboratories (IDEXX, Human 9 and 16 species-specific STR marker profile).

Measurement of stress-induced deformation using the planar-cut method. We slightly modified previous methods[4,9]. The tissue deformation map was acquired via high-resolution ultrasound (Vevo 2100 system; FUJIFILM Visual Sonics) on the half of the tumour–brain that was immersed and relaxed in PBS. We used the probe MS550S for large samples (depth of view = 13 mm, frequency = 32–56 MHz) and the probe MS700 for smaller samples (depth of view = 9 mm, frequency = 30–70 MHz). The three-dimensional (3D) images were exported from VisualSonics software to MATLAB (The MathWorks) for post-processing. The post-processing included smoothing, which was performed with moving averaging on the cut surface and bottom surfaces of the brain tumour to remove any noise introduced by ultrasound imaging. The top and bottom

surfaces were then exported to SolidWorks (Dassault System) to reconstruct a 3D object. This solid object was then exported to the compatible finite-element model ABAQUS (Dassault System), as described below.

Atomic force microscopy-based measurement of the indentation modulus (stiffness). The indentation moduli of tumours and normal brain were quantified using an Asylum MFP3D atomic force microscope (AFM; Asylum). We used polystyrene colloidal probe tips with an end diameter of ~25 µm (Polysciences) attached to tipless cantilevers with nominal spring constant $k \approx 0.12\,\mathrm{N\,m^{-1}}$ (Bruker). The colloidal probes were attached to the cantilever by the lift-off process: a dot of low-viscosity glue (M-Bond 610, Structure Probes/SPI Supplies) was placed on a tipless cantilever by making quick contact between the cantilever and a thin layer of glue (1 µl thick) spread over a 10 × 10 mm mica surface. We then made immediate contact between the tip of the cantilever and a colloid probe resting on a glass slide and waited for 1 min with the cantilever pushing against the colloid. This process was followed by heat curing for 2 h at 150 °C. For each probe tip, the exact spring constants of the cantilevers were directly measured using the thermal calibration method. The relationship between the detected voltage and the applied force was calibrated by bringing the cantilever into contact with a glass slide and calculating the slope of the voltage–displacement curve. The displacement, d, was translated to force, F, using Hooke's law ($F = kd$; k is the cantilever spring constant). The indentation was performed under a force control scheme (maximum force ~20 nN) limiting the indentation depths to 0.5–3 µm to stay in the linear regime. The tip displacement was obtained by subtracting the cantilever deflection from the vertical movement of the piezoelectric actuator. An indentation approach velocity of $2\,\mu\mathrm{m\,s^{-1}}$ ensured that the elastic modulus was probed at rates lower than the characteristic frequency of tumour as a poroelastic tissue[51,52], to be close to equilibrium conditions. The effective indentation modulus E_{ind} was computed using Hertzian contact mechanics models via least-squares linear regression of the experimental loading force–displacement curves. For the spherical colloidal probe tip with end radius R on the sample with thickness $h \gg R$ (here, $h \approx 5$ mm, $R \approx 12.5$ µm)

$$F = \frac{\frac{4}{3}E_{ind}}{1-\nu^2} R^{\frac{1}{2}} D^{\frac{3}{2}}$$

where F is the indentation force and D is the indentation depth (we assumed $\upsilon = 0.1$, as measured in other soft tissues[53,54]).

Despite differences in absolute values, the relative differences between the stiffness of brain parenchyma and tumour tissue are consistent with a previous publication where magnetic resonance elastography (MRE) has been utilized for stiffness measurement[55]. The discrepancies between our AFM measurement and MRE methods are potentially due to: the difference in the measurement methods (Young's modulus is estimated from the indentation modulus in the AFM measurement in quasi-equilibrium indentation, while the MRE is based on measurement of shear wave speed when the tissue is vibrated at a certain frequency, for example, 1,000 Hz[55], which has a strong effect on the reported stiffness values[56]); in vivo versus ex vivo settings (our AFM measurement is performed in vivo, while the MRE has been performed in vivo, when vascular and interstitial fluid pressures are present and may affect the stiffness values[57]); and strain-stiffening effect (our measurements have been performed on stress-relaxed samples, while the stressed tissue may exhibit higher stiffness value due to material nonlinearity[58,59]).

Mathematical model. By developing a mathematical model (2D axisymmetric finite-element model), the map of stress-induced deformation u_i is converted to the strain tensor, $\varepsilon_{ij} = 1/2(\partial u_i/\partial x_j + \partial u_j/\partial x_i)$, from which the stress tensor σ_{ij} is estimated on the basis of Hooke's law, written in index notation as[60]:

$$\sigma_{ij} = \frac{E}{(1+\nu)}\left[\varepsilon_{ij} + \frac{\nu}{(1-2\nu)}\varepsilon_{kk}\delta_{ij}\right]$$

where E is the modulus of elasticity (stiffness), ν is the Poisson ratio of the tissue based on linear isotropic assumption and δ_{ij} is the Kroenecker delta. We chose a linear elastic model to reduce model parameters, and avoid associated assumptions. However, the mathematical model can be improved in multiple directions[1]: the use of hyperelastic models[61] to account for nonlinearity in the material properties of the normal brain tissue and brain tumours (for example, strain-stiffening[58,59] in which stiffness values are altered in stressed tissues); the use of a poroelastic model[1] to account for the role of interstitial, vascular and cerebrospinal fluid pressure; and the use of a triphasic model to account for the electromechanics of brain and tumour tissue with fixed charge density[62].

We developed our mathematical model using the general-purpose commercial finite-element software ABAQUS (Version 6.9, SIMULIA). The 3D geometry of the tumour is first smoothed to reduce any noise in MATLAB (MathWorks). Since the geometries of the tumours of interest are mainly spherical, we used an axisymmetric model (Supplementary Fig. 1d) to reduce the modelling and computational time. We used the eight-node axisymmetric element CAX8R for both the tumour and surrounding brain tissue with two elastic parameters: the Young modulus and the Poisson ratio, which are obtained as described above. We have previously shown that the solid stress relaxation time constant is on the order of 10 min or less[4], following the linear poroelastic time constant predicted from the Young modulus and hydraulic permeability in poroelastic materials[51,63]. Since the time constant of the biological processes that give rise to solid stress in tumours, such as proliferation, extracellular matrix deposition and cell contraction, ranges from several hours to days, much longer than the stress relaxation time constant, the equilibrium mechanical properties that we are measuring reflect the appropriate properties in the generation and application of solid stress.

Since the tumours of interest are all surrounded by the brain tissue, free of solid stress at locations far from the tumour, the cut surface in the brain provides the reference plane that represents the original plane of the tumour tissue before stress relaxation. A displacement profile is assigned to the top deformed surface of the tumour to translate it back to the original reference plane (Supplementary Video 1). This assigned deformation is only in the direction perpendicular to the surface of the tumour (z direction), and the tumour top surface is free to move parallel to the surface direction (x–y plane). This displacement assignment translates the tumour geometry from the relaxed state (deformed surface) to the original stresses state before the cut (flat surface). The stress component σ_{zz} that is generated after the displacement assignment is reported as the circumferential solid stress in the intact brain tumour. The boundary condition on the bottom surface of the surrounding brain tissue, far from the tumour, is defined as zero stress.

We are able to estimate the radial stress σ_{rr} from σ_{zz}, the stress component normal to the cut surface that is obtained from the planar-cut method if the following assumptions hold: the geometry and material properties of the tumour hold spherical symmetry around the centre of the tumour; the incision from the planar cut is going through the centre of the tumour (that is, σ_{zz} is equivalent to $\sigma_{\theta\theta}$); and the stress field goes to zero at the outer edges of the surrounding brain far from the tumour. With the above assumption, the following equation holds between σ_{rr} and $\sigma_{\theta\theta} = \sigma_{zz}$[60]:

$$\frac{\mathrm{d}\sigma_{rr}}{\mathrm{d}r} + \frac{2\sigma_{rr}}{r} = \frac{2\sigma_{\theta\theta}}{r}$$

which results in the following equation after integration:

$$(\sigma_{rr} r^2)\,|_r^{R_0} = \int_r^{R_0} 2\sigma_{\theta\theta} r\,\mathrm{d}r$$

Having $\sigma_{\theta\theta} = \sigma_{zz}$ from the planar-cut method for the range of interest, and assuming $\sigma_{rr} = \sigma_{\theta\theta} = 0$ at $r = R_0$, the outer edge of the brain far from the tumour, the radial stress σ_{rr} is estimated (Fig. 1a,b).

Cranial window. To implant transparent cranial windows, a 6-mm circle was drawn over the frontal and parietal regions of the skull bilaterally. Using a high-speed air-turbine drill with a burr-tip 0.5 mm in diameter, a groove was made on the margin of the drawn circle, until the bone flap became loose. The bone flap was separated from the dura mater underneath. The dura and arachnoid membranes were cut completely from the surface of both hemispheres, avoiding any damage to the sagittal sinus. The window was sealed with a 7-mm cover glass, glued to the bone with histocompatible cyanoacrylate glue.

Tumour implantation. To generate orthotopic tumours, ten days after the cranial window implantation the coverslip was removed and 1 µl of 1–500,000 cells (MGG8, GL261, BT474) was stereotactically and slowly injected with a 28-gauge micro-syringe into the left striatum of 8- to 10-week-old female nude mice 2 mm left of the sagittal suture, 0.1 mm rostral of the bregma, and at a depth of 2 mm from the brain surface. In the case of U87 tumours, 1-mm chunks were implanted in the same region described above. Then a new cover glass was glued on. Of note, the brain tumour models we used are characterized by different degrees of infiltration in the surrounding tissue. Regarding the GBM models, U87 is the most nodular, GL261—although largely nodular—presents a low degree of infiltration and MGG8 is the most infiltrative. While U87 and MGG8 tumours rarely show necrosis when the tumours are not too large, GL261 tumours usually have multiple necrotic regions[48,49]. BT474 tumours are mostly nodular and present necrosis when tumour volumes are large[50].

Immunohistochemistry. Whole heads were collected after intracardiac perfusion with 2% formaldehyde in PBS and then fixed with 2% formaldehyde in PBS for 24–72 h. We next embedded the brains in paraffin, and 5-µm-thick paraffin sections were cut using a microtome and mounted on glass slides. For IHC, tissues were deparaffinized, and antigen retrieval was performed in a pH 9 solution (DAKO) at 96 °C. To prevent nonspecific staining, sections were incubated with 5% normal donkey serum (Jackson ImmunoResearch) in PBS before incubation with the respective primary and secondary antibodies. The primary antibodies used are listed in Supplementary Table 3.

Apoptag (ApopTag Peroxidase In Situ Apoptosis Detection Kit, no. S7100, Millipore) was used as a marker for apoptosis.

The number of neurons in the cortex was assessed by quantifying the number of $NeuN^+$ nuclei in mosaics of the coronal sections of the region of the cortex

exposed to the compression apparatus (that is, the anterior cingulate area, the primary and secondary motor area and the first part of the primary somatosensory area). The structures were identified using the mouse brain atlas map.

Intravital optical frequency domain imaging and perfused vessel analysis. In vivo imaging of perfused vessels and analysis of the vascular fraction and diameter was performed using OCT as previously described[13,64]. OCT assessment was performed at the indicated time until mouse death/euthanasia. The construction, design and algorithms used to derive and quantify OCT images were previously described in detail[13]. In Fig. 2a, we segmented and rendered vessels using a semi-automated algorithm (Bitplane Imaris Image Analysis software).

Multiphoton intravital microscopy. For intravital microscopy, the cranial window-bearing animals were anaesthetized with isoflurane and fixed with a bilateral plastic holder. The multiphoton laser scanning microscope consisted of a MilleniaX pumped Tsunami Ti:sapphire laser (Spectra-Physics). The multiphoton laser scanning microscope consisted of an Olympus Fluoview FV300 system customized for multiphoton imaging. For carboxytetramethylrhodamine (TAMRA) and GFP 810-nm excitation laser light was used, while for EGFP/DsRed/CasadeBlue sequential imaging with 730- and 930-nm excitation laser lights was used. Power at the sample was estimated to be 1–3 mW. The used emission band-pass filters were the following: 610 ± 75 nm for TAMRA/DsRed, 535 ± 43 nm for GFP/EGFP and 413 ± 4 nm for CascadeBlue. We performed vessel angiography after retro-orbital injection of 0.1 ml of 10 mg ml^{-1} TAMRA- or CascadeBlue-tagged dextran (500 kDa; in-house conjugated). The images shown are 3D renderings of high-resolution z stacks: 706 × 706 µm (xy voxel of 0.69) and at least 50 µm of z stack (z steps 2 µm). We segmented and rendered vessels and tumour cells using a semi-automated algorithm (Bitplane Imaris Image Analysis software).

Ultrasound measurements of intracranial tumour volume. To assess tumour size in U87 and BT474 preclinical models, in vivo imaging was performed through plastic cranial windows using a small animal ultrasonography device (Vevo 2100, FujiFilm VisualSonics Inc.).

In vivo lectin perfusion. For lectin perfusion analyses, mice were slowly (~2 min) injected with 100 ml of 1 mg ml^{-1} biotin-conjugated lectin (Vector Labs) via retro-orbital injection 5 min before brain collection, long enough for lectin to reach perfused vessels. Next, we performed 4% formaldehyde heart-perfusion. The brains were then excised, fixed in 4% formaldehyde in PBS overnight and embedded in paraffin blocks[4].

Patient eligibility. *Study A.* Sixty-four previously untreated ('pre-surgical') adult patients (mean age = 62 years; range 32–87; 29 females and 35 males) with a subsequent histologically confirmed diagnosis of a GBM were retrospectively recruited from a cohort of patients examined at our institution[65]. All patients were referred for a conventional MRI examination, including structural and contrast-enhanced perfusion imaging. Evidence of a contrast-enhancing tumour on structural MRI scans (>1 cm in at least one dimension and/or > 10 cm^3) was required. No forms of anticancer medicines or Gliadel wafers were allowed for study inclusion, except for the use of steroids as part of standard-of-care. Other inclusion criteria included a KPS score of >60. Use of steroids and KPS scores were recorded at the time of the MRI exam.

Study B. A second cohort of 14 adult patients (mean age 59 years; range 35–77; 8 females and 6 males) with histologically confirmed newly diagnosed GBM ('post-surgical') at the time of the MRI exam was also retrospectively included[66]. The MRI exams were pulled from the baseline data (pre-therapy) part of an observational imaging study assessing the effects of chemo-radiation monotherapy (clinicalTrials.gov identifier NCT00756106). Except for the post-surgical status, the inclusion criteria matched those of the pre-surgical study described above. A minimum of >1 cm residual tumour in at least one dimension was required and patients with gross total resections were excluded.

Study C. Finally, baseline MRI data from a cohort of 34 patients (mean age 47 years; range 31–62; all females) with metastatic BC to the brain were pulled from an open-label, non-randomized, phase II study on carboplatin and bevacizumab (clinicalTrials.gov identifier NCT01004172). Patients were either HER2-negative (8 patients) or HER2-positive (26 patients). Evidence of a contrast-enhancing tumour on structural MRI scans (>1 cm in at least one dimension) was required. Other inclusion criteria were no contraindication to MRI, an Eastern Cooperative Oncology Group performance status (ECOG PS) of 0–2, no increase in corticosteroid dose in the week before the baseline MR exam, left ventricular ejection fraction >50%, and adequate bone marrow, liver and renal function. Patients could have received prior carboplatin monotherapy. Prior bevacizumab was allowed if it had not been given since or within 6 months before the diagnosis of CNS metastases. Prior radiation therapy to the brain was allowed, conditioned by radiologic confirmation of subsequent brain lesions progression, or presence of one or more untreated residual lesions for analysis in our study. Patients who had not received radiotherapy were allowed if they did not require corticosteroids. There was no limit on the number of prior therapies. A two-week washout period was required from chemotherapy or any other investigational therapy. A one-week washout period was required for lapatinib. No washout period was required for trastuzumab.

All patient studies were approved by the Institutional Review Boards of MGH or Dana-Farber, including the use of informed consent.

MRI acquisition. For all studies, each subject was scanned before the start of therapy. For study A[65], patients were scanned on either a 1.5 Tesla MRI system (Signa; GE Healthcare) or a 3.0 Tesla MRI system (TimTrio, Siemens Healthcare). For studies B and C, all MRI exams were performed at 3.0 Tesla (TimTrio, Siemens Healthcare)[66]. The MRI scans specific for our study were typically as follows.

T2-weighted images. Axial T2-weighted images images with a repetition time (TR) of 4,000 milliseconds (ms), echo time (TE) 104 ms, 5 millimeters (mm) slice thickness, 1 mm inter-slice gap, 0.43 mm in-plane resolution, 19–23 slices and a 512 × 512 image voxel matrix. Axial fluid-attenuated inversion recovery (FLAIR) images with TR 10,000 ms, TE 70 ms, inversion time (TI) 1,500 ms, 5 mm slice thickness, 1 mm inter-slice gap, 0.43 mm in-plane resolution, 23-25 slices and a 512 × 512 image voxel matrix.

T1-weighted images. Axial T1-weighted images acquired before—and after (CE-T1)—injection of contrast agent (gadopentetate-dimeglumine, Gd-DTPA, Magnevist, Bayer Schering Pharma AG). TR 600 ms, TE 12 ms, 5 mm slice thickness, 1 mm inter-slice gap, 0.43 mm in-plane resolution, 23 slices and a 512 × 512 image voxel matrix.

Diffusion images. Axial images using a twice refocused echo-planar diffusion-weighted sequence with TR ~8,000 ms, TE 80–85 ms, low and high b values of 0 s mm^{-2} and 700 s mm^{-2} in 7 and 42 directions, respectively, for diffusion tensor reconstruction. The resolution was 2 mm isotropic, 64 slices and a 128 × 128 image voxel matrix.

Perfusion images. Axial dynamic susceptibility contrast (DSC) images using a gradient-echo echo-planar imaging sequence with TR 1,400–1,500 ms, TE 30–35 ms, flip angle 90°, 5 mm slice thickness, 1.5 mm inter-slice gap, 1.2 mm in-plane resolution, 12 slices and a 160 × 160 image voxel matrix. A total of 100 volumes were acquired and 0.1 mmol kg^{-1} of Gd-DTPA was injected at 5 cm^3 s^{-1} after approximately 81 s of imaging. In addition, for studies B and C as part of a dynamic contrast enhanced image acquisition preceding the dynamic susceptibility contrast imaging, patients also received 0.1 mmol kg^{-1} of Gd-DTPA acting as a pre-dose to minimize computational errors due to T_1-shortening effects induced by contrast agent leakage in regions of blood–brain barrier breakdown or resection.

MRI post-processing. *Volumetrics.* Using a previously described volumetric approach[67], areas of signal intensity abnormality on T2-weighted, FLAIR and CE-T1 images were outlined by an experienced neuroradiologist blinded to the order of the scans. Total tumour volume was estimated by summing all voxels in the enhancing tumour. All images, including the tumour outlines from the second visit, were realigned to the perfusion MR images at the first visit using normalized mutual information coregistration in Matlab (MathWorks).

Diffusion. Apparent diffusion coefficient maps estimating the relative water self-diffusion on a voxel-by-voxel basis were created from the low- and high-b-value images using standard Steskjal–Tanner diffusion approximation[68] as well as measures of fractional anisotropy[69].

Perfusion. Cerebral blood flow maps from the gradient-echo perfusion MRIs were calculated using established models in nordicICE (NordicNeuroLab) and corrected for contrast-agent leakage[70]. Patient-specific variations were reduced by normalization of all brain voxel values to an average value from a normal-appearing grey- and white-matter tissue map excluding pathological areas as identified by the neuroradiologist on the MRIs[71].

Perfusion-gradient analysis. An image voxel-level, unsupervised morphological dilatation in Matlab was performed from the edge of the pathologic area (CE-T1, T2-weighted and FLAIR) and in steps equalling one image voxel growth in all outwards directions (Supplementary Fig. 5a). The algorithm was allowed to grow only in regions with voxels included in the normal-appearing grey- and white-matter tissue map, excluding large vessels, regions of necrosis and/or cysts[71,72]. A stable/increase ('unchanged perf') or reduction ('reduced perf') in the perfusion gradient in the peri-edematous region was defined as being over/below a 5% difference from the average perfusion value of normal-appearing tissue in regions outside a >10 pixel range (>12 mm distance from the peri-edematous zone).

VASARI scoring of MRI. Pre-surgical MRI images for the 64 treatment-naive GBM (Study A) were qualitatively scored for morphological features associated with nodular and infiltrative phenotypes by a board-certified neuroradiologist reader with 10 years of clinical and research experience on brain tumours. The reader was blinded to clinical information (KPS, overall survival) and advanced

MRI data (perfusion metrics) and classified tumours as 'well defined' versus 'poorly defined' according to features f12 and f13 of the VASARI criteria[8] (https://wiki.cancerimagingarchive.net/display/Public/VASARI+Research+Project) utilizing CE-T1, T2-weighted and FLAIR images, respectively. In addition, tumours were scored according to their shape on CE-T1, T2-weighted and FLAIR images utilizing an ordinal four-tier scheme: sphere/oval; sphere/oval + lobulations; irregular; and non-mass or diffuse/patchy. Nodular, well-defined tumours usually grow concentrically and are expected to have more spherical/oval shapes, while infiltrative, poorly marginated tumours are expected to have more irregular or diffuse/patchy appearances.

Compression apparatus model. The compression apparatus is comprised of a polyvinyl chloride (PVC) circular disc (2 mm thick, 7 mm in diameter) acting as a modified cranial window, a stainless-steel set screw (M2x5mm) to apply the controlled chronic displacement on the brain tissue, a PVC membrane (0.01 mm thick) to separate the brain tissue from the set screw and other components, and a custom-made polydimethylsiloxane disc (1 mm thick, 3 mm in diameter) that surrounds the set screw from the top of the window to reduce potential backlash, backing off or loosening of the set screw. All of the components are purchased from McMaster-Carr. The PVC membrane is attached to the edge of the PVC disc by glue. The outer side of the PVC membrane, which is in contact with brain tissue, is clear of any glue to avoid any toxicity. The device is rinsed with ethanol before the surgical procedure.

The compression was performed under gas anaesthesia (isoflurane) every 2–3 days. Each turn of the screw was measured by OCT to be sure that an equal amount of compressing volume was applied to every cortex. No tissue toxicity was detected in brain in contact with the membrane of the compression apparatus. No haemorrhages occurred in any mouse as a consequence of compression or decompression of the cortex. In rare cases of rupture of the membrane of the compression apparatus, the apparatus inevitably fell off the implantation causing a change in intracranial pressure; in those cases, we immediately euthanized and excluded the mice from the study. Mice were checked daily for potential pain and distress. At the end point, each compression apparatus was checked to confirm that no breach of the membrane had occurred.

Histology. Whole heads were collected after intracardiac perfusion with 2% formaldehyde in PBS and then fixed with 2% formaldehyde in PBS for 24–72 h. We next embedded the brains in paraffin, and 5-µm-thick paraffin sections were cut using a microtome and mounted on glass slides. Haematoxylin–eosin (H&E) and cresyl violet (Nissl staining) stains are commonly used histological methods for morphological assessments of the cells in brain tissue. Thus, the paraffin slices were stained with H&E and cresyl violet in the study for histologic evaluation.

Ultrastructural analysis by electron microscopy. Whole heads were collected after intracardiac perfusion with 2% formaldehyde and 2% glutaraldehyde in PBS and then fixed with 2% formaldehyde and 2% glutaraldehyde in PBS for 24–72 h. Vibratome sections (50 µm) of mouse brain were post-fixed in 2.5% glutaraldehyde/PBS for 30 min, washed well in PBS, and treated with 1% osmium tetraoxide/PBS for 1 h, then 1% uranyl acetate/70% ethanol for 45 min. The tissue was then dehydrated in alcohol, embedded in EPON, thin-sectioned on an UltraCut E (Reichert-Jung), and examined using a JEOL JEM-1011 transmission electron microscope with AMTv601 software (Advanced Microscopy Techniques).

RNA isolation and quantitative real-time PCR. Mouse brain tissues were homogenized and total RNA was isolated utilizing the RNeasy Mini kit (Qiagen) according to the manufacturer's protocol. Genomic DNA was removed using the RNase-Free DNase Set (Qiagen). One microgram of RNA was used for the first-strand cDNA synthesis (Bio-Rad). A no-reverse transcriptase control was included in the same PCR mixtures without reverse transcriptase to confirm the absence of DNA contamination in RNA samples. Quantitative real- time PCR (qPCR) primers were synthesized at the MGH DNA core facility (Supplementary Table 4). Reactions (25 µl) were carried out in 96-well optical reaction plates using SYBR Green PCR Master Mix (Bio-Rad) with gene-specific primers, and the qPCR was run in the Stratagene Mx3000p Real-Time PCR System. Amplification of each sample was analysed by melting curve analysis, and relative differences in each PCR sample were corrected using *GAPDH* messenger RNA as an endogenous control and normalized to the level of the control by using the $2^{-\Delta\Delta Ct}$ method as previously described[73,74].

Rotarod test. The neurological function of the mice was assessed by using an automated Rotarod (Rotamex 4/8 4-Lane Treadmill Shock Grid; Columbus Instruments). To exclude the effect of motivational factors and to differentiate between motor learning and actual neurological function, mice were trained on the Rotarod every day for three days. Mice were randomized at the beginning of the study to have the same means in Rotarod endurance. The Rotarod test was performed always at a similar period of the day and after 1 h of acclimation of the mice in the room. We excluded mice that repeatedly fell off very early (<20 s). Tests in two consecutive days were performed for each animal. Each test began with a 30 s acclimation period at 4 r.p.m. followed by acceleration by 4 r.p.m. every 30 s. The latency to fall was recorded as Rotarod endurance[75].

Static gait test. Gait characteristics (stride and track length) were analysed by applying ink to the animals' hind paws and letting them walk on a strip of paper, inside a brightly lit alley (4.5 cm large, 40 cm long), towards a dark goal box. Mice were tested three consecutive times on the day of maximum compression of the cortex (day 12).

Short-term release of the solid stress. The release of the tumour-induced compression of the surrounding tissue was performed by removing the cranial window from anaesthetized mice. This allowed us to obtain a map of the mechanical stress-induced deformation in a brain with or without the nodular U87 tumour. We then checked the dynamics of in vivo perfusion during the process of the release of the tumour-induced compression by OCT. Mice were then euthanized.

Therapeutic neuroprotection treatments. Mice were randomized at the beginning of the study by Rotarod endurance. We systemically treated mice with the following drugs during the chronic/gradual compression and the two following weeks after decompression: necrostatin-1 (7 mg kg^{-1} d^{-1} i.p.; similar to ref. [26]), valproic acid (400 mg kg^{-1} d^{-1} i.p.[27]) and lithium chloride (50 mg kg^{-1} d^{-1} i.p.[28]). All of these drugs are known to cross the blood–brain barrier[31–33] and shown to be neuroprotective during CNS ischaemia or neurodegeneration[26–28]. In the case of dexamethasone, the steroid anti-edema drug was given once (10 mg kg^{-1}; refs. [29,30]) at the day of maximum compression (day 14). In the case of lithium treatment 'intervention study' (that is, with treatment start when compression was already applied to the brains), lithium chloride (50 mg kg^{-1} d^{-1} i.p.[28]) was given from day 10 after the chronic compression initiation.

RNA-Seq. RNA-Seq was performed by the Massachusetts Institute of Technology BioMicro Center. The quality of RNA samples was confirmed using a fragment analyser (Advanced Analytical Technologies, Inc.) before Illumina libraries were prepared and indexed from ~250 ng of total RNA using the Kapa Hyperprep kit following the manufacturer's recommendations (Roche). Libraries were confirmed using the fragment analyser and quantified by qPCR before pooling and sequencing on an Illumina NextSeq500 using 40 + 40 paired end reads. Samples were demultiplexed using custom scripts allowing a single mismatch to the index sequencing.

Analysis of RNA-Seq data. The raw FASTQ files were aligned by STAR[76] to the Ensembl GRCm38 reference genome. Gene read counts were then generated using the Bioconductor R package GenomicAlignments[77]. The Bioconductor R package DESeq2[78] was then used to normalize and determine the differentially expressed genes. The DAVID Bioinformatics Resource[34] was used for gene-annotation enrichment analysis on the differentially expressed genes.

Statistical analysis. Unless otherwise specified, the data are presented as the mean ± s.e.m. Student's two-tailed *t*-tests based on Gaussian distributions were used to assess the significance. For comparisons among more than two groups, analysis of variance or Kruskal–Wallis tests were followed by post hoc multiple comparisons. $P < 0.05$ was considered significant. For comparison between categorical datasets, Fisher's test was performed. Blinding during analysis was used for all of the experiments and clinical analyses. Statistics were performed using Graphpad Prism or Microsoft Excel. A detailed list of the performed tests is provided in Supplementary Table 5.

Reporting Summary. Further information on research design is available in the Nature Research Reporting Summary linked to this article.

Code availability. The computer codes used in this study are available from the corresponding author upon reasonable request.

Data availability

The authors declare that all data supporting the findings of this study are available within the paper and its Supplementary Information. Raw RNA-Seq data from this study have been deposited in the NCBI Sequence Read Archive (SRA) under submission ID SUB4405185 and BioProject ID PRJNA486395.

Received: 22 December 2017; Accepted: 25 November 2018;
Published online: 07 January 2019

References

1. Goriely, A. et al. Mechanics of the brain: perspectives, challenges, and opportunities. *Biomech. Model. Mechanobiol.* **14**, 931–965 (2015).
2. Helmlinger, G., Netti, P. A., Lichtenbeld, H. C., Melder, R. J. & Jain, R. K. Solid stress inhibits the growth of multicellular tumor spheroids. *Nat. Biotechnol.* **15**, 778–783 (1997).
3. Stylianopoulos, T. et al. Causes, consequences, and remedies for growth-induced solid stress in murine and human tumors. *Proc. Natl Acad. Sci. USA* **109**, 15101–15108 (2012).

4. Nia, H. T. et al. Solid stress and elastic energy as measures of tumour mechanopathology. *Nat. Biomed. Eng.* **1**, 0004 (2016).
5. Jain, R. K., Martin, J. D. & Stylianopoulos, T. The role of mechanical forces in tumor growth and therapy. *Annu. Rev. Biomed. Eng.* **16**, 321–346 (2014).
6. Chauhan, V. P. et al. Compression of pancreatic tumor blood vessels by hyaluronan is caused by solid stress and not interstitial fluid pressure. *Cancer Cell* **26**, 14–15 (2014).
7. Stylianopoulos, T. et al. Coevolution of solid stress and interstitial fluid pressure in tumors during progression: implications for vascular collapse. *Cancer Res.* **73**, 3833–3841 (2013).
8. Gamburg, E. S. et al. The prognostic significance of midline shift at presentation on survival in patients with glioblastoma multiforme. *Int. J. Radiat. Oncol. Biol. Phys.* **48**, 1359–1362 (2000).
9. Nia, H. T. et al. Quantifying solid stress and elastic energy from excised or in situ tumors. *Nat. Protoc.* **13**, 1091–1105 (2018).
10. Mazurowski, M. A., Desjardins, A. & Malof, J. M. Imaging descriptors improve the predictive power of survival models for glioblastoma patients. *Neuro. Oncol.* **15**, 1389–1394 (2013).
11. Chambless, L. B. et al. The relative value of postoperative versus preoperative Karnofsky Performance Scale scores as a predictor of survival after surgical resection of glioblastoma multiforme. *J. Neurooncol.* **121**, 359–364 (2015).
12. Chauhan, V. P. et al. Angiotensin inhibition enhances drug delivery and potentiates chemotherapy by decompressing tumour blood vessels. *Nat. Commun.* **4**, 2516 (2013).
13. Vakoc, B. J. et al. Three-dimensional microscopy of the tumor microenvironment in vivo using optical frequency domain imaging. *Nat. Med.* **15**, 1219–1223 (2009).
14. Bar-Kochba, E., Scimone, M. T., Estrada, J. B. & Franck, C. Strain and rate-dependent neuronal injury in a 3D in vitro compression model of traumatic brain injury. *Sci. Rep.* **6**, 30550 (2016).
15. Arundine, M., Aarts, M., Lau, A. & Tymianski, M. Vulnerability of central neurons to secondary insults after in vitro mechanical stretch. *J. Neurosci.* **24**, 8106–8123 (2004).
16. Field, A. S. et al. Diffusion tensor eigenvector directional color imaging patterns in the evaluation of cerebral white matter tracts altered by tumor. *J. Magn. Reson. Imaging* **20**, 555–562 (2004).
17. Blanchet, L. et al. Discrimination between metastasis and glioblastoma multiforme based on morphometric analysis of MR images. *AJNR Am. J. Neuroradiol.* **32**, 67–73 (2011).
18. Takano, T. et al. Glutamate release promotes growth of malignant gliomas. *Nat. Med.* **7**, 1010–1015 (2001).
19. Balkaya, M., Krober, J. M., Rex, A. & Endres, M. Assessing post-stroke behavior in mouse models of focal ischemia. *J. Cereb. Blood Flow Metab.* **33**, 330–338 (2013).
20. Roth, L. et al. Impaired gait pattern as a sensitive tool to assess hypoxic brain damage in a novel mouse model of atherosclerotic plaque rupture. *Physiol. Behav.* **139**, 397–402 (2015).
21. Budday, S. et al. Mechanical characterization of human brain tissue. *Acta Biomater.* **48**, 319–340 (2017).
22. Budday, S. et al. Mechanical properties of gray and white matter brain tissue by indentation. *J. Mech. Behav. Biomed. Mater.* **46**, 318–330 (2015).
23. Johnson, C. L. et al. Local mechanical properties of white matter structures in the human brain. *Neuroimage* **79**, 145–152 (2013).
24. Ohue, S. et al. Evaluation of intraoperative brain shift using an ultrasound-linked navigation system for brain tumor surgery. *Neurol. Med. Chir.* **50**, 291–300 (2010).
25. Paul, D. A. et al. White matter changes linked to visual recovery after nerve decompression. *Sci. Transl. Med.* **6**, 266ra173 (2014).
26. Yang, S. H. et al. Nec-1 alleviates cognitive impairment with reduction of Abeta and tau abnormalities in APP/PS1 mice. *EMBO Mol. Med.* **9**, 61–77 (2017).
27. Dash, P. K. et al. Valproate administered after traumatic brain injury provides neuroprotection and improves cognitive function in rats. *PLoS ONE* **5**, e11383 (2010).
28. Makoukji, J. et al. Lithium enhances remyelination of peripheral nerves. *Proc. Natl Acad. Sci. USA* **109**, 3973–3978 (2012).
29. Rocksen, D., Lilliehook, B., Larsson, R., Johansson, T. & Bucht, A. Differential anti-inflammatory and anti-oxidative effects of dexamethasone and N-acetylcysteine in endotoxin-induced lung inflammation. *Clin. Exp. Immunol.* **122**, 249–256 (2000).
30. Capasso, A., Di Giannuario, A., Loizzo, A., Pieretti, S. & Sorrentino, L. Dexamethasone pretreatment reduces the psychomotor stimulant effects induced by cocaine and amphetamine in mice. *Prog. Neuro-Psychopharmacol. Biol. Psychiatry* **19**, 1063–1079 (1995).
31. Forester, B. P. et al. Brain lithium levels and effects on cognition and mood in geriatric bipolar disorder: a lithium-7 magnetic resonance spectroscopy study. *Am. J. Geriatr. Psychiatry* **17**, 13–23 (2009).
32. Phiel, C. J. et al. Histone deacetylase is a direct target of valproic acid, a potent anticonvulsant, mood stabilizer, and teratogen. *J. Biol. Chem.* **276**, 36734–36741 (2001).
33. Jagtap, P. G. et al. Structure–activity relationship study of tricyclic necroptosis inhibitors. *J. Med. Chem.* **50**, 1886–1895 (2007).
34. Huang da, W., Sherman, B. T. & Lempicki, R. A. Systematic and integrative analysis of large gene lists using DAVID bioinformatics resources. *Nat. Protoc.* **4**, 44–57 (2009).
35. Can, A. et al. Antidepressant-like responses to lithium in genetically diverse mouse strains. *Genes Brain Behav.* **10**, 434–443 (2011).
36. Moore, G. J., Bebchuk, J. M., Wilds, I. B., Chen, G. & Manji, H. K. Lithium-induced increase in human brain grey matter. *Lancet* **356**, 1241–1242 (2000).
37. Foland, L. C. et al. Increased volume of the amygdala and hippocampus in bipolar patients treated with lithium. *Neuroreport* **19**, 221–224 (2008).
38. Rowe, M. K. & Chuang, D. M. Lithium neuroprotection: molecular mechanisms and clinical implications. *Expert Rev. Mol. Med.* **6**, 1–18 (2004).
39. Yazlovitskaya, E. M. et al. Lithium treatment prevents neurocognitive deficit resulting from cranial irradiation. *Cancer Res.* **66**, 11179–11186 (2006).
40. Yu, F. et al. Lithium ameliorates neurodegeneration, suppresses neuroinflammation, and improves behavioral performance in a mouse model of traumatic brain injury. *J. Neurotrauma* **29**, 362–374 (2012).
41. Li, Q. et al. Lithium reduces apoptosis and autophagy after neonatal hypoxia-ischemia. *Cell Death Dis.* **1**, e56 (2010).
42. Han, S. et al. Lithium enhances the antitumour effect of temozolomide against TP53 wild-type glioblastoma cells via NFAT1/FasL signalling. *Br. J. Cancer* **116**, 1302–1311 (2017).
43. Korur, S. et al. GSK3β regulates differentiation and growth arrest in glioblastoma. *PLoS ONE* **4**, e7443 (2009).
44. Nowicki, M. O. et al. Lithium inhibits invasion of glioma cells; possible involvement of glycogen synthase kinase-3. *Neuro. Oncol.* **10**, 690–699 (2008).
45. Meyers, C. A. & Brown, P. D. Role and relevance of neurocognitive assessment in clinical trials of patients with CNS tumors. *J. Clin. Oncol.* **24**, 1305–1309 (2006).
46. Wakimoto, H. et al. Maintenance of primary tumor phenotype and genotype in glioblastoma stem cells. *Neuro. Oncol.* **14**, 132–144 (2012).
47. Griveau, A. et al. A glial signature and Wnt7 signaling regulate glioma–vascular interactions and tumor microenvironment. *Cancer Cell* **33**, 874–889 e877 (2018).
48. Kloepper, J. et al. Ang-2/VEGF bispecific antibody reprograms macrophages and resident microglia to anti-tumor phenotype and prolongs glioblastoma survival. *Proc. Natl Acad. Sci. USA* **113**, 4476–4481 (2016).
49. Peterson, T. E. et al. Dual inhibition of Ang-2 and VEGF receptors normalizes tumor vasculature and prolongs survival in glioblastoma by altering macrophages. *Proc. Natl Acad. Sci. USA* **113**, 4470–4475 (2016).
50. Askoxylakis, V. et al. Preclinical efficacy of ado-trastuzumab emtansine in the brain microenvironment. *J. Natl Cancer Inst.* **108**, djv313 (2016).
51. Nia, H. T., Han, L., Li, Y., Ortiz, C. & Grodzinsky, A. Poroelasticity of cartilage at the nanoscale. *Biophys. J.* **101**, 2304–2313 (2011).
52. Netti, P. A., Berk, D. A., Swartz, M. A., Grodzinsky, A. J. & Jain, R. K. Role of extracellular matrix assembly in interstitial transport in solid tumors. *Cancer Res.* **60**, 2497–2503 (2000).
53. Kiviranta, P. et al. Collagen network primarily controls Poisson's ratio of bovine articular cartilage in compression. *J. Orthop. Res.* **24**, 690–699 (2006).
54. Buschmann, M. D. et al. Stimulation of aggrecan synthesis in cartilage explants by cyclic loading is localized to regions of high interstitial fluid flow. *Arch. Biochem. Biophys.* **366**, 1–7 (1999).
55. Jamin, Y. et al. Exploring the biomechanical properties of brain malignancies and their pathologic determinants in vivo with magnetic resonance elastography. *Cancer Res.* **75**, 1216–1224 (2015).
56. Arani, A. et al. Acute pressure changes in the brain are correlated with MR elastography stiffness measurements: initial feasibility in an in vivo large animal model. *Magn. Reson. Med.* **79**, 1043–1051 (2018).
57. Weickenmeier, J. et al. Brain stiffens post mortem. *J. Mech. Behav. Biomed. Mater.* **84**, 88–98 (2018).
58. Pogoda, K. et al. Compression stiffening of brain and its effect on mechanosensing by glioma cells. *New J. Phys.* **16**, 075002 (2014).
59. Storm, C., Pastore, J. J., MacKintosh, F. C., Lubensky, T. C. & Janmey, P. A. Nonlinear elasticity in biological gels. *Nature* **435**, 191–194 (2005).
60. Timoshenko, S. & Goodier, J. *Theory of Elasticity* (McGraw-Hill Book Company, New York, 1951).
61. Mihai, L. A., Chin, L., Janmey, P. A. & Goriely, A. A comparison of hyperelastic constitutive models applicable to brain and fat tissues. *J. R. Soc. Interface* **12**, 20150486 (2015).
62. Lang, G. E., Stewart, P. S., Vella, D., Waters, S. L. & Goriely, A. Is the Donnan effect sufficient to explain swelling in brain tissue slices? *J. R. Soc. Interface* **11**, 20140123 (2014).
63. Grodzinsky, A. J. *Fields, Forces, and Flows in Biological Systems* (Garland Science, New York, 2011).
64. Ager, E. I. et al. Blockade of MMP14 activity in murine breast carcinomas: implications for macrophages, vessels, and radiotherapy. *J. Natl Cancer Inst.* **107**, djv017 (2015).

65. Emblem, K. E. et al. A generic support vector machine model for preoperative glioma survival associations. *Radiology* **275**, 228–234 (2015).
66. Pinho, M. C. et al. Low incidence of pseudoprogression by imaging in newly diagnosed glioblastoma patients treated with cediranib in combination with chemoradiation. *Oncologist* **19**, 75–81 (2014).
67. Sorensen, A. G. et al. Comparison of diameter and perimeter methods for tumor volume calculation. *J. Clin. Oncol.* **19**, 551–557 (2001).
68. Oh, J. et al. Quantitative apparent diffusion coefficients and T2 relaxation times in characterizing contrast enhancing brain tumors and regions of peritumoral edema. *J. Magn. Reson. Imaging* **21**, 701–708 (2005).
69. Basser, P. J. & Pierpaoli, C. Microstructural and physiological features of tissues elucidated by quantitative-diffusion-tensor MRI. *J. Magn. Reson. B* **111**, 209–219 (1996).
70. Bjornerud, A. & Emblem, K. E. A fully automated method for quantitative cerebral hemodynamic analysis using DSC-MRI. *J. Cereb. Blood Flow Metab.* **30**, 1066–1078 (2010).
71. Emblem, K. E. & Bjornerud, A. An automatic procedure for normalization of cerebral blood volume maps in dynamic susceptibility contrast-based glioma imaging. *AJNR Am. J. Neuroradiol.* **30**, 1929–1932 (2009).
72. Emblem, K. E., Due-Tonnessen, P., Hald, J. K. & Bjornerud, A. Automatic vessel removal in gliomas from dynamic susceptibility contrast imaging. *Magn. Reson. Med.* **61**, 1210–1217 (2009).
73. Ren, J. et al. Protein kinase C-delta (PKCdelta) regulates proinflammatory chemokine expression through cytosolic interaction with the NF-kappaB subunit p65 in vascular smooth muscle cells. *J. Biol. Chem.* **289**, 9013–9026 (2014).
74. Vitner, E. B. et al. RIPK3 as a potential therapeutic target for Gaucher's disease. *Nat. Med.* **20**, 204–208 (2014).
75. Gao, X. et al. Anti-VEGF treatment improves neurological function and augments radiation response in NF2 schwannoma model. *Proc. Natl Acad. Sci. USA* **112**, 14676–14681 (2015).
76. Dobin, A. et al. STAR: ultrafast universal RNA-seq aligner. *Bioinformatics* **29**, 15–21 (2013).
77. Lawrence, M. et al. Software for computing and annotating genomic ranges. *PLoS Comput. Biol.* **9**, e1003118 (2013).
78. Love, M. I., Huber, W. & Anders, S. Moderated estimation of fold change and dispersion for RNA-seq data with DESeq2. *Genome Biol.* **15**, 550 (2014).

Acknowledgements

We thank A. Ivinson (UK Dementia Research Institute), M. A. Moskowitz and M. J. Whalen (MGH) for critical discussion and insightful suggestions; S. Roberge, M. Duquette, C. Smith and E. L. Jones (MGH) for technical support, H. Wakimoto (MGH) for the MGG8 cell line and O. Rapalino (MGH) for help with the pre-operative clinical study. This work was supported by the National Cancer Institute (NCI; P01-CA080124, P50-CA165962, R01-CA129371, R01-CA208205, U01-CA 224348), NCI Outstanding Investigator Award (R35-CA197743), the Lustgarten Foundation, the Ludwig Center at Harvard, the National Foundation for Cancer Research and the Gates Foundation (R.K.J), R01-HL128168 (to J.W.B., T.P.P. and L.L.M.), DP2OD008780 (T.P.P.), R01CA214913 (T.P.P.), P41EB015903 (Center for Biomedical OCT Research and Translation), NIH/NINDS P30NS045776 (EM facility core) and P30-CA14051 from NCI (Koch Institute Genomics core). This work was also supported in part by the Susan G. Komen Foundation Fellowship PDF14301739, Fondation ARC pour la recherche sur le cancer and the INSERM-CNRS ATIP-Avenir grant (G.S.), NCI F32-CA216944-01 (H.T.N.), the European Research Council (ERC) under the European Union's Horizon 2020 (grant agreement no. 758657), the South-Eastern Norway Regional Health Authority grants 2017073, 2016102 and 2013069, the Research Council of Norway grants 261984 and ES435705, the Norwegian Cancer Society grants 6817564 and 3434180 (K.E.E.), F31HL126449 from the National Heart, Lung, and Blood Institute at the NIH (M.D.), SolidarImmun fellowship (J.K.), Feodor-Lynen Postdoctoral Fellowship from Alexander von Humboldt Foundation (M.G.) and Deutsche Forschungsgemeinschaft AS422-2/1 (V.A.).

Author contributions

G.S., H.T.N. and K.E.E. conceived the project and wrote the manuscript; G.S. conducted most of the experiments, performed data analysis and generated most of the experimental mice; H.T.N. designed and developed the in vivo compression device and conducted the biomedical engineering experiments; K.E.E. designed the patient stratification method and analysed the perfusion MRIs; J.K., L.R. and V.A. performed OCT intravital angiography experiments on multiple models; M.D., J.R., S.K. and M.G. assisted with histological analyses, preclinical models and pharmacological treatments; M.C.P. blindly classified the clinical cohorts using the VASARI features; W.W.H. analysed RNA-Seq results; G.B.F. provided expertise on the neuroscience parts of the manuscript; E.R.G., T.T.B., P.Y.W. and N.U.L. provided MRI images and patients' characteristics from clinical trials; A.J.G., D.F., P.H., J.W.B., T.P.P. and L.L.M. contributed to discussions on crucial aspects of the project and drafted the manuscript; R.K.J. supervised the project and provided guidance on experimental design, data interpretation and writing of the manuscript.

Competing interests

R.K.J. received an honorarium from AMGEN and consultant fees from Pfizer, Ophthotech, Merck, SPARC, SynDevRx and XTuit. R.K.J. owns equity in Enlight, Ophthotech and SynDevRx, and serves on the Boards of Trustees of Tekla Healthcare Investors, Tekla Life Sciences Investors, the Tekla Healthcare Opportunities Fund and the Tekla World Healthcare Fund. No reagents or funding from these companies was used in these studies. K.E.E. has intellectual properties with NordicNeuroLab AS, Bergen, Norway.

Additional information

Supplementary information is available for this paper at https://doi.org/10.1038/s41551-018-0334-7.

Reprints and permissions information is available at www.nature.com/reprints.

Correspondence and requests for materials should be addressed to R.K.J.

Publisher's note: Springer Nature remains neutral with regard to jurisdictional claims in published maps and institutional affiliations.

nature research

Corresponding author(s): Rakesh K. Jain

Reporting Summary

Nature Research wishes to improve the reproducibility of the work that we publish. This form provides structure for consistency and transparency in reporting. For further information on Nature Research policies, see Authors & Referees and the Editorial Policy Checklist.

Statistical parameters

When statistical analyses are reported, confirm that the following items are present in the relevant location (e.g. figure legend, table legend, main text, or Methods section).

n/a	Confirmed	
☐	☒	The exact sample size (*n*) for each experimental group/condition, given as a discrete number and unit of measurement
☐	☒	An indication of whether measurements were taken from distinct samples or whether the same sample was measured repeatedly
☐	☒	The statistical test(s) used AND whether they are one- or two-sided *Only common tests should be described solely by name; describe more complex techniques in the Methods section.*
☒	☐	A description of all covariates tested
☐	☒	A description of any assumptions or corrections, such as tests of normality and adjustment for multiple comparisons
☐	☒	A full description of the statistics including central tendency (e.g. means) or other basic estimates (e.g. regression coefficient) AND variation (e.g. standard deviation) or associated estimates of uncertainty (e.g. confidence intervals)
☐	☒	For null hypothesis testing, the test statistic (e.g. *F*, *t*, *r*) with confidence intervals, effect sizes, degrees of freedom and *P* value noted *Give P values as exact values whenever suitable.*
☒	☐	For Bayesian analysis, information on the choice of priors and Markov chain Monte Carlo settings
☒	☐	For hierarchical and complex designs, identification of the appropriate level for tests and full reporting of outcomes
☒	☐	Estimates of effect sizes (e.g. Cohen's *d*, Pearson's *r*), indicating how they were calculated
☐	☒	Clearly defined error bars *State explicitly what error bars represent (e.g. SD, SE, CI)*

Our web collection on statistics for biologists may be useful.

Software and code

Policy information about availability of computer code

Data collection	Images were collected with imaging software, such as Zen lite for IHC, Vevo VisualSonics for ultrasound, Olympus FluoView for confocal and multi-photon, AMTv601 software for TEM, nordicICE v3 for MRI and a custom-made software for OCT (as previously described in Vakoc, Nat Med, 2009).
Data analysis	The following commercial software were used to analyze the results: VisualSonics software, SolidWorks, ABAQUS Version 6.9, Bitplane Imaris 7.0 Image Analysis software, Graphpad Prism 7, Microsoft Excel and ImageJ. Moreover, we used previously published MATLAB and ImageJ custom algorithms. The computer codes are available from the corresponding author upon reasonable request.

For manuscripts utilizing custom algorithms or software that are central to the research but not yet described in published literature, software must be made available to editors/reviewers upon request. We strongly encourage code deposition in a community repository (e.g. GitHub). See the Nature Research guidelines for submitting code & software for further information.

Data

Policy information about availability of data

All manuscripts must include a data availability statement. This statement should provide the following information, where applicable:

- Accession codes, unique identifiers, or web links for publicly available datasets
- A list of figures that have associated raw data
- A description of any restrictions on data availability

The authors declare that all data supporting the findings of this study are available within the paper and its supplementary information. Raw RNA-sequencing data from this study have been deposited in the NCBI Sequence Read Archive (SRA) under submission ID SUB4405185 and BioProject ID PRJNA486395.

Field-specific reporting

Please select the best fit for your research. If you are not sure, read the appropriate sections before making your selection.

☒ Life sciences ☐ Behavioural & social sciences ☐ Ecological, evolutionary & environmental sciences

For a reference copy of the document with all sections, see nature.com/authors/policies/ReportingSummary-flat.pdf

Life sciences study design

All studies must disclose on these points even when the disclosure is negative.

Sample size	No sample-size calculation was performed because all animal studies were built with the maximum technically feasible number of animals. Because of the surgical complexities in cranial window and compression-device implantation, in practice sample sizes could only be 6–8 per experiment.
Data exclusions	No data were excluded from the presented analyses.
Replication	Each result presented is at least a duplicate of experiments or animal studies. All attempts at replication were successful.
Randomization	Mice were randomized by pre-treatment Rotarod endurance and body weight.
Blinding	Blinding during analysis was used for all the experiments and clinical analyses.

Reporting for specific materials, systems and methods

Materials & experimental systems

n/a	Involved in the study
☒	☐ Unique biological materials
☐	☒ Antibodies
☐	☒ Eukaryotic cell lines
☒	☐ Palaeontology
☐	☒ Animals and other organisms
☐	☒ Human research participants

Methods

n/a	Involved in the study
☒	☐ ChIP-seq
☒	☐ Flow cytometry
☐	☒ MRI-based neuroimaging

Antibodies

Antibodies used	Rat anti-Coll IV (EMD Millipore; AB7569), mouse anti-NeuN (Chemicon, MAB377), rabbit anti-GFP (Cell Signaling Technology, #2956), rabbit anti-HER2 (Cell Signaling Technology, #2165), rabbit anti-CC3 (Cell Signaling Technology, mAb #9664), rabbit anti-LC3-II (Cell Signaling Technology, #12741), rabbit anti-GFAP (DAKO, Z0334), mouse anti-CNPase (Millipore, MAB326). Apoptag (ApopTag Peroxidase In Situ Apoptosis Detection Kit, #S7100, Millipore) was used as a marker for apoptosis. Specifications are listed in Table S3.
Validation	The used antibodies are all well-established and validated as described in the manufacturer's websites.

Eukaryotic cell lines

Policy information about cell lines

Cell line source(s)	The human U87 and BT474 cells were from ATCC and the mouse Gl261 cells were from the National Cancer Institute Repository. MGG8, a cell line derived from a GBM patient, was previously established in the Department of Neurosurgery at Massachusetts General Hospital (Dr. Hiroaki Wakimoto, MGH).
Authentication	All cell lines were authenticated before use by IDEXX Laboratories (IDEXX , Human 9 and 16 species-specific STR marker profile)
Mycoplasma contamination	All cell lines were repeatedly tested and were negative for mycoplasma using the Mycoalert Plus Mycoplasma Detection Kit (Lonza).
Commonly misidentified lines (See ICLAC register)	No commonly misidentified cell lines were used.

Animals and other organisms

Policy information about studies involving animals; ARRIVE guidelines recommended for reporting animal research

Laboratory animals	All animal protocols were approved by and in accordance with the guidelines established by the Institutional Animal Care and Use Committee (IACUC) at Massachusetts General Hospital (MGH). The mouse colony (MGH Cox7) was maintained in accordance with National Institutes of Health and MGH guidelines. MGH is accredited with the International Association for Assessment and Accreditation of Laboratory Animal Care (AAALAC) and the NIH Office of Laboratory Animal Welfare (A3596-01). All experiments were performed in 8 to 10 week-old female nude mice. In the case of Figure 2D, we used CAG::H2B-EGFP (C57/BL6) mice from Jackson Laboratory.
Wild animals	The study did not involve wild animals.
Field-collected samples	The study did not involve samples collected from the field.

Human research participants

Policy information about studies involving human research participants

Population characteristics	Study A: Sixty-four previously untreated ("pre-surgical") adult patients (mean age= 62 years; range 32-87; 29 females and 35 males) with a subsequent histologically confirmed diagnosis of a glioblastoma were retrospectively recruited from a cohort of patients examined at our institution. All patients were referred for a conventional MRI examination, including structural and contrast-enhanced perfusion imaging. Evidence of contrast-enhancing tumor on structural MRI scans (>1cm in at least one dimension and/or > 10cc) was required. No forms of anti-cancer medicines or Gliadel wafers were allowed for study inclusion, except for the use of steroids as part of standard-of-care. Other inclusion criteria included a Karnofsky Performance Status (KPS) score of >60. Use of steroids and KPS scores were recorded at the time of the MRI exam. Study B: A second cohort of 14 adult patients (mean age 59 years; range 35-77; 8 females and 6 males) with histologically confirmed newly diagnosed glioblastomas ('post-surgical') at the time of the MRI exam was also retrospectively included13. The MRI exams were pulled from the baseline data (pre-therapy) part of an observational imaging study assessing the effects of chemo-radiation monotherapy (clinicalTrials.gov identifier NCT00756106). Except for the post-surgical status, the inclusion criteria matched that of the pre-surgical study described above. A minimum of >1cm residual tumor in at least one dimension was required and patients with gross total resections were excluded. Study C: Finally, baseline MRI data from a cohort of 34 patients (mean age 47 years; range 31-62; all females) with metastatic breast cancer to the brain were pulled from an open-label, non-randomized, phase II study on carboplatin and bevacizumab (clinicalTrials.gov identifier NCT01004172). Patients were either HER2-negative (8 patients) or HER2-positive (26 patients). Evidence of contrast-enhancing tumor on structural MRI scans (>1cm in at least one dimension) was required. Other inclusion criteria were no contraindication to MRI, an Eastern Cooperative Oncology Group performance status (ECOG PS) of 0-2, no increase in corticosteroid dose in the week prior to the baseline MR exam, left ventricular ejection fraction >50%, and adequate bone marrow, liver and renal function. Patients could have received prior carboplatin monotherapy. Prior bevacizumab was allowed if it had not been given since or within 6 months prior to the diagnosis of CNS metastases. Prior radiation therapy to the brain was allowed, conditioned by radiologic confirmation of subsequent brain lesions progression, or presence of one or more untreated residual lesions for analysis in our study. Patients who had not received radiotherapy were allowed if they did not require corticosteroids. There was no limit on the number of prior therapies. A two-week washout period was required from chemotherapy or any other investigational therapy. A one-week washout period was required for lapatinib. No washout period was required for trastuzumab.
Recruitment	All patient studies were approved by the Institutional Review Board, including the use of informed consent.

Magnetic resonance imaging

Experimental design

Design type	Clinical MRI exams as part of the pre-treatment (surgery or therapy) work-up.

Design specifications

Full clinical MR imaging protocol of patients later confirmed to have brain the cancers (primary glioblastoma or brain metastasis from breast cancer). For all patients, a single MRI exam prior to surgery or therapy was included in the study. The full MRI protocol took approximately 1:00-1:30 (hours:minutes).

Behavioral performance measures

No behavioral performance was tested. These were clinical MRI exams.

Acquisition

Imaging type(s)

Anatomical and functional/dynamic (diffusion and perfusion MRI)

Field strength

Patients with primary brain tumors {glioblastomas) were scanned on either a 1.5 Tesla MRI system (Signa;GE Healthcare) or a 3.0 Tesla MRI system (TimTrio,Siemens Healthcare). For patients with brain metastases, all MRI exams were performed at 3.0 Tesla (TimTrio, Siemens Healthcare)

Sequence & imaging parameters

The MRI scans specific for our study were as follows:
1. FLAIR images: Axial images with a repetition time (TR) 10000ms, echo time (TE) 70ms, 5mm slice thickness, 1mm inter-slice gap, 0.43mm in- plane resolution, 23 slices and a 512x512 matrix.
2. T1 images: AxialTl-weighted images acquired prior to- and after-injection of contrast agent (gadopentetate-dimeglumine, Gd-DTPA, Magnevist, Bayer Schering Pharma AG, Berlin, Germany). TR 600ms, TE 12ms, 5mm slice thickness, 1mm inter-slice gap, 0.43mm in-plane resolution, 23 slices and a 512x512 matrix.
3. Diffusion images: Axial images using a twice refocused echo-planar
diffusion weighted sequence with TR 8000ms, TE 80-85 ms, low and high b-values of 0s/mm2 and 700s/mm2 in 7 and 42 directions, respectively, for diffusion tensor reconstruction. Resolution was 2 mm isotropic, 64 slices and a 128x128 matrix.
4. Perfusion images: Axial dynamic susceptibility contrast (DSC) images using a gradient-echo echo-planar imaging sequence with TR 1400-1500ms, TE 30-35ms, flip angle 90*, 5mm slice thickness, 1.5mm inter-slice gap, 1.2mm in-plane resolution, 12 slices and a 160x160 matrix. A total of 100 volumes were acquired and 0.1mmol/kg of Gd-DTPA was injected at 5cc/s after approximately 81s of imaging. In addition,for studies B and C as part of a dynamic contrast enhanced image acquisition preceding the DSC imaging, patients also received a 0.1mmol/kg of Gd- DTPA acting as a pre-dose to minimize computational errors due to T1- shortening effects induced by contrast agent leakage in regions of blood- brain barrier breakdown or resection.

Area of acquisition

Pathologic regions (brain tumor, edematous region) were manually defined by a expert neuroradiologist. Subsequent whole-brain regions for contrast were identified by automatic analysis of perfusion MRI (Emblem KE,et al, Magn Reson Med 2008 and Emblem KE, et al, AJNR 2009) taking care to exclude the radiologist-defined pathologic regions.

Diffusion MRI ☒ Used ☐ Not used

Parameters

Axial images using a twice refocused echo-planar diffusion weighted sequence with TR 8000ms, TE 80-85ms, low and high b-values of 0s/mm2 and 700s/mm2 in 7 and 42 directions, respectively, for diffusion tensor reconstruction. Resolution was 2 mm isotropic, 64 slices and a 128x128 matrix

Preprocessing

Preprocessing software

MRI data preprocessing (including perfusion and diffusion analysis): nordicICE version 3.
Region volume outlining: nordicICE version 3 and 3DSlicer version 3
Perfusion gradient analysis: Matlab version R2013b

Normalization

Normalization of all relative MRI data (perfusion and diffusion) data was performed by making ratio value maps from each image voxel value to a mean value of the normal-appearing reference tissue as described in Emblem KE, et al. AJNR 2009.

Normalization template

Data was not transformed to a template space- please refer comment above (7.a.)

Noise and artifact removal

Dynamic data (perfusion MRI) was motion corrected using rigid body coregistration to the first image time point using nordiciCE as part of the preprocessing routine. The temporal signal was smoothened with a gaussian filter to remove spikes in single image time points (volumes) of the 80-100 volume series.

Volume censoring

Only MRI exams with a full protocol according to the standard clinical protocol were included. There was no additional volume censoring following the radiologists approval of image quality.

Statistical modeling & inference

Model type and settings

Not applicable. Mean values from the entire ROI only.

Effect(s) tested

An unsupervised morphological dilatation (in Matlab R2013b) was performed from the edge ofthe pathologic area (tumor and edema) and in steps equaling one image voxel growth in all outwards directions. The algorithm was only allowed to grow in regions with voxels included in the normal-appearing brain tissue maps (ref section 5), excluding large vessels, regions of necrosis and/or cysts (Emblem KE, et al, Magn Reson Med 2008).A stable/increase ("unchanged perf") or reduction ("reduced perf") in the perfusion gradient in the peri-edematous region was defined as being over/below a 5% difference from the average perfusion value of normal-appearing tissue in regions outside a >10 pixels range (>12mm distance from the peri-edematous zone).

Specify type of analysis: ☐ Whole brain ☐ ROI-based ☒ Both

Anatomical location(s)	ROI-based (tumor and edematous) and whole-brain as described in sections 5 and 11. Tha anatomical locations were determined by an expert neuroradiologist.
Statistic type for inference (See Eklund et al. 2016)	Not applicable.
Correction	Holm-Bonferroni was performed in the case of multiple comparisons.

Models & analysis

n/a	Involved in the study
☒	☐ Functional and/or effective connectivity
☒	☐ Graph analysis
☒	☐ Multivariate modeling or predictive analysis